Original article

Dual-targeted halofuginone hydrobromide nanocomplexes for promotion of macrophage repolarization and apoptosis of rheumatoid arthritis fibroblast-like synoviocytes in adjuvant-induced arthritis in rats

Junping Zhu [a, 1], Ye Lin [a, 1], Gejing Li [a], Yini He [a], Zhaoli Su [a], Yuanyuan Tang [a, b], Ye Zhang [a], Qian Xu [a], Zhongliu Yao [a], Hua Zhou [c, ***], Bin Liu [b, **], Xiong Cai [a, *]

[a] Institute of Innovation and Applied Research in Chinese Medicine; Department of Rheumatology of First Hospital, Hunan University of Chinese Medicine, Changsha, 410208, China
[b] College of Biology, Hunan University, Changsha, 410082, China
[c] State Key Laboratory of Traditional Chinese Medicine Syndrome, Guangdong Provincial Hospital of Chinese Medicine, Guangdong Provincial Academy of Chinese Medical Sciences, The Second Affiliated Hospital of Guangzhou University of Chinese Medicine, Guangzhou, 510006, China

A B S T R A C T

Rheumatoid arthritis (RA) is a prevalent autoimmune disease characterized by chronic inflammation and excessive proliferation of the synovium. Currently, treatment options focus on either reducing inflammation or inhibiting synovial hyperplasia. However, these modalities are unsatisfactory in achieving the desired therapeutic outcomes. Halofuginone hydrobromide (HF), an herbal active ingredient, has demonstrated pharmacological effects of both anti-inflammation and inhibition of synovial hyperplasia proliferation. However, HF's medical efficacy is limited due to its poor water solubility, short half-life ($t_{1/2}$), and non-target toxicity. In the current study, by using the advantages of nanotechnology, we presented a novel dual-targeted nanocomplex, termed HA-M@P@HF NPs, which consisted of a hyaluronic acid (HA)-modified hybrid membrane (M)-camouflaged poly lactic-*co*-glycolic acid (PLGA) nanosystem for HF delivery. These nanocomplexes not only overcame the limitations of HF but also achieved simultaneous targeting of inflammatory macrophages and human fibroblast-like synoviocytes-RA (HFLS-RA). *In vivo* experiments demonstrated that these nanocomplexes effectively suppressed immune-mediated inflammation and synovial hyperplasia, safeguarding against bone destruction in rats with adjuvant-induced arthritis (AIA). Remarkable anti-arthritic effects of these nanocomplexes were accomplished through promoting repolarization of M1-to-M2 macrophages and apoptosis of HFLS-RA, thereby offering a promising therapeutic strategy for RA.

© 2024 The Author(s). Published by Elsevier B.V. on behalf of Xi'an Jiaotong University. This is an open access article under the CC BY-NC-ND license (http://creativecommons.org/licenses/by-nc-nd/4.0/).

1. Introduction

Rheumatoid arthritis (RA) is a persistent and complex systemic condition affecting 0.25%−1% of the global population [1]. It is characterized by sustained inflammation and hyperplasia of the synovium, leading to cartilage and bone damage [2]. Central to the pathology of RA are macrophages and human fibroblast-like synoviocytes-like RA (HFLS-RA) [3]. The inflammatory environment exerts dual harmful effects, such as direct erosion of cartilage and bone through catabolic activities and stimulation of abnormal proliferation and division of HFLS-RA [4]. Current RA treatments include nonsteroidal anti-inflammatory drugs (NSAIDs), disease-modifying anti-rheumatic drugs (DMARDs), biologic agents, and glucocorticoids [5]. However, these drugs based therapy often fails to control symptoms in many RA patients. For example, PEGylated tumor necrosis factor (TNF)-inhibitors have 57% effectiveness but 56% adverse events, like infections [6,7]. Janus kinase (JAK) inhibitors, while beneficial, come with side effects such as nausea,

cardiovascular events, infections, and malignancies [8]. Therefore, there is a pressing need for innovative therapies for enhancing efficacy in the treatment of RA while minimizing non-targeted side effects.

Halofuginone hydrobromide (HF), a quinazolinone alkaloid extracted from the Chinese herb *Dichroa febrifuga* Lour. (Fig. S1), modulates immune responses and mitigates joint damage in RA [9]. Additionally, HF hinders the TNF-α-induced migration and proliferation of HFLS-RA, controlling synovial inflammation and hyperplasia [10], and inhibits the interleukin-17 (IL-17) signaling pathway of macrophages to exert an inhibitory effect on RA immune inflammation [5]. In our primary study, we revealed that HF could exert anti-inflammatory effects by promoting phenotypic transformation in macrophages and curbs synovial hyperplasia by inducing HFLS-RA apoptosis. Despite these promising attributes, transitioning HF into a viable clinical therapy faces several challenges including short half-life ($t_{1/2}$), limited solubility, low bioavailability, and side effects [11]. Addressing these limitations is crucial for enhancing the clinical utility of HF in the treatment of RA.

In theory, the rational integration of nanoparticles (NPs) with HF can overcome these inherited disadvantages of HF and improve drug efficacy by targeted delivering drug into RA joints. Among the various NP options, poly lactic-*co*-glycolic acid NPs (PLGA NPs) are clinically approved drug carriers [12] with biocompatibility and high drug-loading efficiency [13] (Table S1). However, the rapid clearance of uncoated nanodrugs by immune system results in a short circulatory $t_{1/2}$, limiting drug concentration at targeted sites [14]. Cell membrane coatings was reported to augment nanodrug functionalities, such as circulation time and targeted delivery [15]. Red blood cell membrane (RBCm) enhance immune evasion, thereby prolonging circulation [16]. Macrophage membrane (Møm) improve targeting to inflamed joints and synovium access [17]. In light of this, we have developed a biomimetic nanoplatform using both RBCm and Møm.

In this study, we have successfully developed a novel nanosystem with HF (Scheme 1A) for dual-targeting inflammatory macrophages and HFLS-RA to enhance the therapeutic effect on RA (Scheme 1B). HF was encapsulated in PLGA to produce P@HF NPs. Subsequently, a hybrid membrane (M) of RBCm and Møm coated these nanocomplexes, resulting in M@P@HF NPs. This M enhanced the circulation longevity and targeting of the NPs. Additionally, considering the high expression of CD44 on synovial macrophages and HFLS-RA, hyaluronic acid (HA) was chosen as a ligand for CD44 to target dysregulated macrophages and HFLS-RA in rheumatoid synovium. This nanocomposite modulated immune inflammation and synovial hyperplasia, mainly attributed to the synergistic effects of M1-to-M2 macrophage repolarization and HFLS-RA apoptosis. As a result, this innovative nanosystem provided substantial protection for the bone tissue in rats with adjuvant-induced arthritis (AIA), showcasing its potential as an effective treatment modality for RA.

2. Materials and methods

2.1. Patients and sample collection

Samples were collected from 30 randomly selected patients diagnosed with RA and 30 healthy volunteers. The recruitment period took place from March 2022 throughout July 2023 at the First Hospital of Hunan University of Chinese Medicine (HNUCM), China as part of the approved clinical protocols (Approval No.: HN-LL-YJSLW-2023-027) sanctioned by the Ethics Committee of the First Hospital of HNUCM. The diagnosis of RA relied on clinical, radiologic, and/or histopathologic evidence.

2.2. Orthogonal experimental design

A standardized orthogonal table was employed in the design of the orthogonal experiment [18]. Instead of testing all possible combinations, a set of representative parameter combinations was selected to ensure more accurate and reliable results with fewer trials. Four important factors, namely polyvinyl alcohol (PVA) concentration (%, m/V), PLGA/HF ratio (m/m), water-to-oil (W/O) ratio (V/V), and rotation speed (rpm), were determined based on the material preparation process. Levels for each factor were established in accordance with the actual preparation process. An $L9(4^3)$ orthogonal array was chosen for the three-level experiment with the four factors (Table S2). Analysis of variance was subsequently employed to examine the impact of various process parameters on the entrapment efficiency (EE). The significance level of each factor was determined through ranking, which allowed for the identification of the optimal combination of process parameters for material preparation.

2.3. Materials

HF was procured from Target Molecule Co., Ltd. (Shanghai, China). PLGA (50:50, molecular weight 38,000−54,000), lipopolysaccharide (LPS), 3-(4,5-dimethylthiazol-2-yl)-2,5-diphenyltetrazolium bromide (MTT), *N*-hydroxysuccinimide (NHS), and 4′,6-diamidino-2′-phenylindole (DAPI) were sourced from Sigma-Aldrich (Shanghai, China); HA from Dalian Meilun Technology Co., Ltd. (Dalian, China); Hoechst 33342, bicinchoninic acid (BCA) kit, terminal deoxynucleotidyl transferase-mediated nick end labeling (TUNEL) kit, lysosomal staining agent, 1,1′-dioctadecyl-3,3,3′,3′-tetramethylindocarbocyanine perchlorate (DiI), and 3,3′-dioctadecyloxacarbocyanine perchlorate (DiO) from Yeasen Biotech (Shanghai, China). PVA with a molecular weight of 9,000−10,000 was procured from Shanghai Macklin Biochemical Co., Ltd. (Shanghai, China). Chlorin e6 (Ce6) was acquired from Shanghai Yuanye Bio-Technology Co., Ltd. (Shanghai, China); dimethyl sulfoxide (DMSO) and 1-ethyl-3-(3-dimethylaminopropyl) carbodiimide (EDC) from Beijing Solarbio Science & Technology Co., Ltd. (Beijing, China); membrane protein extraction kits and loading buffer from Beyotime Biotechnology (Shanghai, China); phosphate-buffered saline (PBS) from Seven Innovation Biological Technology Co., Ltd. (Beijing, China). Fetal bovine serum (FBS) was sourced from Zhejiang Tianhang Biotechnology Co., Ltd. (Huzhou, China). We also utilized antibodies for glyceraldehyde-3-phosphate dehydrogenase (GAPDH), P53, P21, Bcl-2-associated X protein (BAX), Bcl-2, CD80, CD206, Ki67, CD44, CD11b, and CD47, obtained from Proteintech Group Inc. (Wuhan, China).

Cell lines, such as RAW264.7 (mouse macrophages cell line), human umbilical vein endothelial cell (HUVEC), vascular smooth muscle cell (VSMC), rat cardiac myoblast cell (H9C2), human kidney cell (HK2), and human liver cell (HL7702) were acquired from the Cell Library of Xiangya Central Laboratory, Central South University, Changsha, China. HFLS and HFLS-RA were obtained from BeNa Culture Collection. RAW264.7 cells were cultured with 100 ng/mL LPS for 24 h to generate activated macrophages.

Male Sprague-Dawley (SD) rats (Certified No.: 110011221109063828) were purchased at the Beijing Vital River Laboratory Animal Technology Co., Ltd. (Beijing, China). Animals were accommodated at the Laboratory Animal Center of HNUCM, China (License No.: SYXK [Hunan] 2019-0009). Throughout the study, the rats had unrestricted access to food and water. Animal experimental protocols, including their care, were reviewed and approved by the Institutional Animal Care and Use Committee of HNUCM (Ethical No.: LL2022091304). All procedures involving these animals were strictly adhered to the guidelines set by the U.S. National Institute of Health's Guide for the Care and Use of Laboratory Animals.
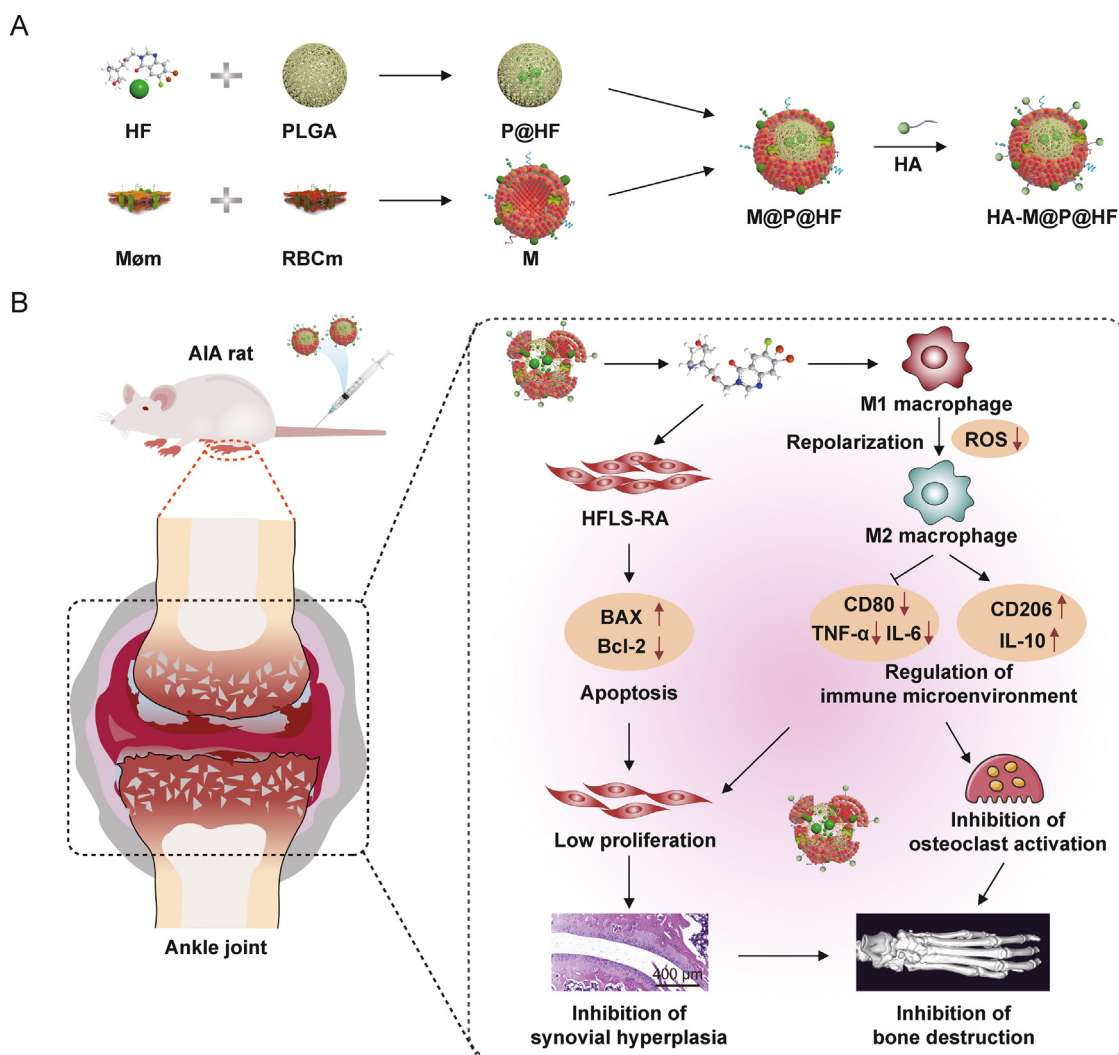
Scheme 1. Schematic preparation of hyaluronic acid (HA)-modified hybrid membrane (M)-camouflaged poly lactic-*co*-glycolic acid (PLGA) loaded halofuginone hydrobromide (HF) nanoparticles (NPs) (HA-M@P@HF NPs) and the strategy for rheumatoid arthritis (RA) treatment. (A) Preparation scheme of HA-M@P@HF NPs. (B) HA-M@P@HF NPs markedly modulated immune inflammation and synovial hyperplasia through the synergistic effects of M1-to-M2 macrophage repolarization and human fibroblast-like synoviocytes-RA (HFLS-RA) apoptosis, thereby protecting adjuvant-induced arthritis (AIA) rats from bone damage for effective RA treatment. Møm: macrophage membrane; RBCm: red blood cell membrane; BAX: Bcl-2-associated X protein; ROS: reactive oxygen species; TNF-α: tumor necrosis factor-α; IL-6: interleukin-6.

2.4. Preparation of M

The extraction of RBCm was conducted following a methodology previously established in our research [19]. For the preparation of Møm, we utilized membrane protein extraction kits. To create the M, RBCm and Møm solutions were combined in a specified weight ratio, subjected to sonication for 15 min, and then hybridized using magnetic stirring at 37 °C for 1 h.

2.5. Preparation of targeting molecule

The synthesis of the targeting molecule HA-polyethylene glycol 2000 (PEG2000)-1,2-distearoyl-*sn*-glycero-3-phosphorylethanolamine (DSPE) was carried out as per the methodology outlined in our earlier research [20]. The process began by mixing 50 mg of NHS, 25 mg of EDC, and 5 mg of HA in PBS. This mixture was stirred at 25 °C for 30 min. Following this, 25 mg of DSPE-PEG2000-NH$_2$ was introduced into the mixture and stirred continuously at 37 °C for another 30 min. The mixture was then allowed to stir at 25 °C for 24 h. The resulting HA-PGE2000-DSPE solution underwent dialysis using a dialysis bag with a molecular weight cutoff (MWCO) of 2,500 Da and was subsequently lyophilized.

2.6. Preparation of HA-M@P@HF NPs

The P@HF NPs were synthesized using a nanoprecipitation technique. Initially, HF and PLGA were dissolved in DMSO. This solution was then sonicated for 5 min to create the oil phase. Gradually, this oil phase was added to a PVA solution under magnetic stirring, followed by dialysis against water for 12 h using a dialysis bag with a MWCO of 2,500 Da. Subsequently, the P@HF NPs were freeze-dried with a protectant for storage. For the M coating, a

solution containing M and the P@HF NPs was stirred at 37 °C for 2 h, leading to the formation of M@P@HF NPs. Excess, uncoated membrane material was removed by centrifugation at 3,000 g, and the sample was washed repeatedly until no proteins were detected in the supernatant. Finally, HA-PEG2000-DSPE was incorporated into the membrane, and HA-M@P@HF NPs were obtained after removing free HA-PEG2000-DSPE.

2.7. Characterization of membrane protein

Sodium dodecyl sulfate-polyacrylamide gel electrophoresis (SDS-PAGE) and Western blot analyses were conducted to identify membrane proteins. Protein samples from RBCm, Møm, M, and HA-M@P@HF NPs were extracted using the Cell Total Protein Extraction kits (Beyotime Biotechnology). The protein samples were mixed with a loading buffer and heated at 95 °C for 5 min. Subsequently, equal amounts of protein were loaded and separated using 10% SDS-PAGE, initially at 80 V for 30 min, followed by 120 V for 1.5 h. One gel was stained with Coomassie bright blue for 2 h and then washed overnight for imaging. The proteins from the other gel were transferred onto a polyvinylidene fluoride (PVDF) membrane. The PVDF membrane was incubated with primary antibodies targeting CD11b (a key marker of Møm) and CD47 (a surface marker of both RBCm and Møm) overnight at 4 °C, followed by a 2 h room temperature incubation with a horseradish peroxidase-labeled secondary antibody. The protein signals were then detected utilizing a ChemiDoc MP imaging system (Bio-Rad, Hercules, CA, USA).

2.8. Characterization of prepared NPs

The P@HF NPs and HA-M@P@HF NPs were imaged using a JEM-2100 Plus transmission electron microscope (TEM). Fourier transform infrared spectroscopy (FT-IR) was employed to analyze the chemical bonds of the NPs. The size and potential of the PLGA NPs, P@HF NPs, and HA-M@P@HF NPs were measured using dynamic light scattering (DLS) (Nano ZS90 Zetasizer, Malvern, Worcestershire, UK). To assess stability, the HA-M@P@HF NPs solution was incubated in 10% FBS for three days, and the size was measured at different time points using DLS.

2.9. In vitro release and release kinetics studies

The drug release of HA-M@P@HF NPs was evaluated using the dialysis method in two different pH media, namely pH 5.4 and 7.4. The HA-M@P@HF NPs solution was placed in a dialysis bag (MWCO = 3,500 Da) and immersed in 10 mL of PBS at 37 °C. The ultraviolet-visible spectroscopy (UV-vis) (UV-1800; Shimadzu, Kyoto, Japan) was then employed to measure the concentration of HF in the PBS at various time points. The cumulative release rate of HF was calculated using the following formula:

$$\text{Cumulative drug release (\%)} = \frac{m_t}{m_o} \times 100\%$$

where m_t is the mass of the drug released in PBS and m_o is the initial mass of the drug in the NPs.

To investigate the kinetic mechanism of HF release from the HA-M@P@HF NPs, the obtained data were analyzed using the zero-order, first-order, Higuchi, Peppas, and Weibull equations with the assistance of OriginPro 2021 software [21]. The linear least-squares fitting method was employed to determine the parameters for each equation, and the quality of fit was evaluated based on the correlation factor (R^2).

2.10. Biocompatibility assays in vitro

The biocompatibility of HA-M@P@HF NPs was assessed using coagulation, hemolysis, and cytotoxicity assays, following a previously established protocol [22]. Platelet (PLT)-rich plasma was obtained from healthy adult SD rats for the coagulation assay. Subsequently, various NPs were incubated with the PLT-rich plasma at 37 °C for 1 h. The absorbance values at 650 nm were measured using a microplate reader.

In the hemolysis assay, various NPs were combined with 4% RBC (V/V) in PBS for 6 h. Afterward, the supernatants were obtained through centrifugation at 3,000 rpm for 5 min, and the sample values at 562 nm were measured using a microplate reader. Additionally, the impact of NPs on the morphology of RBC was examined using a phase contrast microscope (IX-73; Olympus, Tokyo, Japan).

The MTT assay was employed to assess the cytotoxicity of various formulations. RAW264.7, HFLS, VSMC, HUVEC, HL7702, HK2, and H9C2 cells were seeded onto a 96-well plate. Subsequently, different concentrations of P@HF NPs and HA-M@P@HF NPs were introduced into the wells, and the cells were incubated for an additional 24 h. The formula for calculating cell viability is as follows:

$$\text{Cells viability} = \frac{\text{OD}_{490} \text{ of sample}}{\text{OD}_{490} \text{ of control}} \times 100\%$$

2.11. Cell uptake behavior

Macrophages, activated macrophages, HFLS, HFLS-RA, and HUVEC cells were cultured in a 12-well plate for 24 h. Following this, HA-M@P@Ce6 NPs were added and incubated for an additional 4 h. Afterward, the cells were washed three times with PBS and counterstained with Hoechst 33342 for 15 min. Finally, the cells were imaged utilizing confocal laser scanning microscope (CLSM) (FV1200; Olympus).

A series of preincubation steps were employed using various inhibitors to explore the uptake mechanism of HA-M@P@HF NPs by activated macrophages. Initially, activated macrophages were treated with 2-deoxy-d-glucose (2-DG; an inhibitor of energy metabolism), methyl-β-cyclodextrin (β-CD; an inhibitor of caveolae-mediated endocytosis), chlorpromazine (Chlor; an inhibitor of clathrin-dependent endocytosis), and colchicine (Colch; an inhibitor of macropinocytosis) for 1 h. Following this pre-treatment, the cells were exposed to a HA-M@P@Ce6 NP solution, which replaced the existing culture medium. After a 4-h incubation, the cells were imaged for fluorescence utilizing CLSM.

To assess the intracellular distribution of HA-M@P@HF NPs, activated macrophages were treated with HA-M@P@Ce6 for 1, 2, 4, and 8 h. Subsequently, these cells were exposed to a lysosomal staining agent for 30 min. For nuclear visualization, the cells were stained with Hoechst 33342. The final observation and imaging of the cells were conducted using a CLSM.

2.12. Regulation of immune-inflammation in vitro

For the reactive oxygen species (ROS) analysis, RAW264.7 cells were cultured in 12-well plates for 24 h and then treated with either PBS (as a control), HF at a concentration of 2 nM, or HA-M@P@HF NPs (containing 2 nM HF) for 2 h. Then, RAW264.7 cells were co-incubated with 100 ng/mL LPS for 4 h. For post-treatment, both the test and control cells were stained using ROS detection kits (Yeasen Biotech) for 30 min and subsequently examined using a CLSM.

For the detection of inflammatory markers, RAW264.7 cells in 24-well plates were exposed to HA-M@P@HF NPs for 2 h and then

co-incubated with 100 ng/mL LPS for an additional 24 h. After that, the culture media were collected, and the levels of TNF-α, IL-6, and IL-10 were measured utilizing an enzyme-linked immunosorbent assay (ELISA) kit (Neobioscience Biotechnology Co., Ltd., Shenzhen, China).

In the macrophage polarization study, RAW264.7 cells were first stimulated with 500 ng/mL LPS for 24 h and then treated with different agents (PBS, HF, or HA-M@P@HF NPs) for an additional 24 h. After that, the macrophages were harvested, fixed, and incubated with CD80 and CD206 antibodies for 12 h at 4 °C. The media were then replaced with fluorescence-conjugated secondary antibody, and the cells were cultured for a further 2 h. Following this, the cells were washed with PBS and images were captured utilizing a CLSM. The proportions of M1- and M2-type macrophages were subsequently quantified utilizing the ImageJ software.

2.13. In vitro anti-synovitis assay

For the cell viability assay, the cytotoxic effect of HA-M@P@HF NPs on HFLS-RA was evaluated using the MTT assay. In brief, HFLS-RA were seeded at a density of 5×10^3 cells per well in 96-well plates and cultured for 24 h. These cells were then treated for 48 h with either PBS (as a control), HF at a concentration of 0.2 μM, or HA-M@P@HF NPs containing an equivalent concentration of HF. The MTT assay was subsequently performed to assess cell cytotoxicity.

Cells cultured in six-well plates were exposed to PBS, HF, or HA-M@P@HF NPs for cell cycle analysis. Following a 48-h treatment period, the cells were harvested and fixed in 70% (V/V) ethanol for 24 h. Afterward, they were stained using a standard cell cycle detection kit (Beyotime Biotechnology) and analyzed employing flow cytometry of CytoFLEX (Beckman Coulter, Brea, CA, USA).

For the apoptosis analysis using flow cytometry, HFLS-RA were seeded in six-well plates and then treated with either PBS, HF, or HA-M@P@HF NPs. Following a 48-h incubation, apoptosis was assessed according to the protocols provided by the manufacturer of the apoptosis detection kit (Yeasen Biotech).

In the Western blot analysis, HFLS-RA were subjected to treatments with PBS, HF, and HA-M@P@HF NPs. After a 48-h incubation, proteins were separated using SDS-PAGE and then transferred onto PVDF membranes. The membranes were blocked using tris-buffered saline with Tween 20 (TBST) containing 5% skim milk, followed by overnight incubation at 4 °C with primary antibodies targeting GAPDH, P53, P21, BAX, and Bcl-2. Subsequently, the membranes were washed and incubated with secondary antibodies for 2 h at ambient temperature. Finally, the membranes were washed again, and the proteins were detected employing the ChemiDoc XRS system (Bio-Rad) for chemiluminescence visualization.

The following methodology was adopted to evaluate the impact of an M1 macrophage inflammatory environment on the viability of HFLS-RA: RAW264.7 cells were first stimulated with 100 ng/mL LPS for 24 h. These cells were then treated with different formulations (PBS, HF, or HA-M@P@HF NPs) for 24 h. After treatment, the cells were centrifuged at 1,500 rpm for 10 min to separate them from the culture medium. The supernatants from these M1 macrophages, containing the respective treatments, were then applied to HFLS-RA for 48 h. The cell viability post-treatment was assessed utilizing the MTT assay.

2.14. In vivo pharmacokinetics and biodistribution of HA-M@P@Ce6 NPs

The AIA rats were intravenously administered with Ce6, P@Ce6 NPs, or HA-M@P@Ce6 NPs, each at 5 mg/kg Ce6. Subsequent to the injection, blood samples (0.2 mL) were collected from the jugular veins at time intervals of 0, 0.5, 1, 2, 4, 6, 8, 12, 24, and 48 h. The plasma obtained from these samples was then analyzed utilizing an in vivo imaging system (IVIS) (PerkinElmer, Waltham, MA, USA). Additionally, 48 h after the injection, various organs were collected, including the heart, liver, spleen, lung, kidney, brain, and paw tissues. These tissue samples were then subjected to imaging and semi-quantitative analysis to evaluate the biodistribution of the administered compounds.

2.15. Detection of circulating HA-M@P@HF NPs in AIA rats using ultra-performance liquid chromatography tandem mass spectrometry (UPLC-MS/MS)

In this experiment, AIA rats received an intravenous injection of a single dose of either 0.25 mg/kg HF, P@HF, or HA-M@P@HF NPs. Blood samples were collected from the rats' jugular veins at specific intervals post-HF administration: 0, 0.5, 1, 2, 4, 6, 8, 12, 24, and 48 h. These samples were then centrifuged at 3,500 rpm at 4 °C for 10 min. The resulting plasma aliquots were preserved at −80 °C. After 48 h from the injection, vital organs such as the heart, liver, spleen, lung, kidney, brain, and paw tissues were collected. These tissues were processed into homogenates and stored at −80 °C. The concentration of HF in these samples was quantitatively measured utilizing UPLC-MS/MS (AB SCIEX, Waltham, MA, USA).

2.16. In vivo anti-arthritic study

Our study used AIA rats, a standard model for studying RA [23]. Male SD rats received a subcutaneous injection at the tail base with 0.1 mL of complete Freund's adjuvant (CFA). This CFA contained 300 μg of ground, heat-killed Mycobacterium tuberculosis H37Ra (Becton Dickinson, Franklin Lakes, NJ, USA) in mineral oil (Sigma-Aldrich). Starting from the day of CFA administration, the rats were given intravenous injections of either PBS, HF (0.25 mg/kg), PLGA NPs (1.74 mg/kg), or HA-M@P@HF NPs (0.25 mg/kg HF and 1.74 mg/kg PLGA) into the tail vein at three-day intervals until the experiment concluded. A group of AIA rats treated with methotrexate (MTX) at 1 mg/kg orally on days 0, 3, 7, 14, 21, 28, and 35 post CFA injection acted as the positive control group. Rats in the normal control group received similar PBS injections. The severity of arthritis in the rats was assessed every three days after the onset of the condition, using an arthritis scoring system, along with measurements of bi-hind paw volumes and body weight.

Quantum GX micro-computed tomography (CT) imaging (PerkinElmer) was employed to assess bone damage in the hind paws. Following the conclusion of the study, the rats were humanely euthanized using isoflurane inhalation, allowing for the collection of hind paw specimens and blood samples. The collected hind paws were fixed in 4% paraformaldehyde (Beijing Labgic Technology, Beijing, China) and subsequently decalcified using an ethylenediamine tetraacetic acid (EDTA) solution (Beijing Solarbio Science & Technology Co., Ltd.) prior to paraffin embedding. Histological examinations were performed using various staining methods: hematoxylin-eosin (H&E) for lymphocyte (LYM) infiltration, safranin O-fast green (SO-FG) for cartilage assessment, Masson's trichrome for collagen fiber analysis, and tartrate resistant acid phosphatase (TRAP) for osteoclast identification. In immunohistochemistry studies, paw sections were treated with antibodies against Ki67 and CD44. For immunofluorescence, joint sections were incubated with CD80, CD206, ROS markers (Beijing Solarbio Science & Technology Co., Ltd.), or TUNEL assay reagents. Quantitative analyses of these samples were conducted using ImageJ software. Concurrently, blood samples were assayed for IL-6, TNF-α, and IL-10 levels.

2.17. In vivo safety evaluation

Post-treatment blood samples from AIA rats were drawn into tubes coated with EDTA and promptly subjected to analysis with a Sysmex TEK-VET3 automated hematology analyzer (Sysmex Co., Ltd., Kobe, Hyogo, Japan). Concurrently, plasma samples collected in heparin-coated tubes were assessed for liver and kidney function markers using a Roche Cobas C501 automated analyzer (Roche, Basel, Switzerland). Additionally, paraffin-embedded sections of various organs were stained with H&E for histopathological examination.

2.18. Statistical analysis

Data were presented as the mean ± standard deviation from independent experiments. Student's two-sided t-test was used to calculate the difference between two groups. One-way analysis of variance (ANOVA) with multiple comparisons using least significant difference (LSD) was used to analyze differences between different groups. All statistical analyses were conducted using the GraphPad Prism 8.0 software. A threshold of $P < 0.05$ was set for statistical significance.

3. Results and discussion

3.1. Immune-inflammation of patients with RA

The pathogenesis of RA is characterized by pronounced inflammatory responses involving activated macrophages and excessive proliferation of HFLS-RA [24]. These activated macrophages adapt their phenotype in response to the local tissue microenvironment, differentiating into either classically activated (M1) or alternatively activated (M2) macrophages [25,26]. M1 macrophages, which appear in the inflammation and immune responses, release a high level of pro-inflammatory cytokines like TNF-α and IL-6. This leads to synovial hyperplasia, tissue infiltration, and both synovial and bone tissue destruction [27]. Conversely, M2 macrophages, known for secreting anti-inflammatory cytokines such as IL-10, play a role in inhibiting M1 macrophage activation. They cooperatively maintain immune homeostasis and protect joint tissues [28]. Predominantly, RA patients' synovium is characterized by an overabundance of M1 macrophage, creating a state of immune-mediated inflammation [25]. In RA, the disturbed inflammatory environment contributes to the uncontrolled proliferation of HFLS-RA, leading to aggressive tissue destruction and erosion of cartilage and bone [29]. To investigate the change in immune inflammation of RA patients, we collected blood samples from 30 healthy volunteers and 30 RA patients, and analyzed them using human ELISA kit (Jiangsu Meimian Industrial Co., Ltd., Yancheng, China). Interestingly, the results of these samples simultaneously demonstrated the differentially elevated levels of M1 macrophages' markers (TNF-α and IL-6) and M2 macrophages' marker (IL-10) in RA patients as compared to those in the healthy controls (Figs. 1A–C). These data, which are consistent with previous studies [30,31], demonstrated the disrupted inflammatory state in RA. The same upregulation tendency for molecular markers of both M1 and M2 macrophages suggested the complication and dynamic immune response in RA. In addition, ultrasound examination of RA patients' knees and CT of the hands revealed pronounced synovial thickening, cartilage erosion, and bone loss in affected joints (Figs. 1D and E). This result demonstrated that unproper immune response not only leads to the deterioration of synovial tissue and bone loss but also accelerates the aberrant
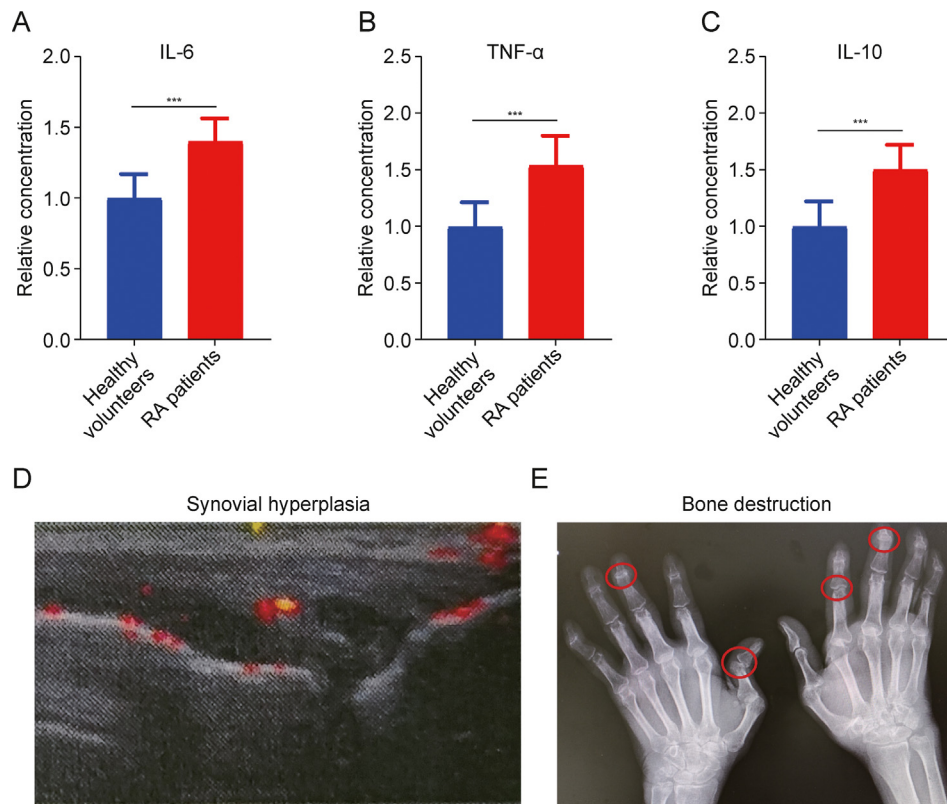

Fig. 1. Pathological inflammatory response in patients with rheumatoid arthritis (RA). (A–C) Enzyme-linked immunosorbent assay (ELISA) detection of interleukin-6 (IL-6) (A), tumor necrosis factor-α (TNF-α) (B), and IL-10 (C) in serum of healthy volunteers and RA patients. (D) Ultrasound of the knees of RA patients showed prominent synovial hyperplasia. (E) Computed tomography (CT) of the hands of RA patients exhibited significant bone damage. Data are presented as mean ± standard deviation ($n = 30$). ***$P < 0.001$.

proliferation of HFLS-RA, exacerbating damage to cartilage and bone [32]. Therefore, it is hypothesized that a treatment strategy, which concurrently targets and induces the repolarization of M1 to M2 macrophages, along with eliminating HFLS-RA, can be a comprehensive solution for RA management.

3.2. Preparation and characterization of HA-M@P@HF NPs

Exploring the effect of HF on the macrophage inflammatory marker TNF-α, it was found a marked increase for TNF-α levels in macrophages with LPS stimulation. However, the following treatment with 2 nM and 4 nM HF resulted in a reduction of TNF-α by approximately 14.57% and 31.38%, respectively (Fig. 2A). Furthermore, MTT assay revealed that HF treatment reduced the viability of HFLS-RA in a dose-dependent manner (Fig. 2B). These findings suggested that HF effectively suppressed macrophage-mediated immune inflammation and the growth and activity of HFLS-RA. Despite its efficacy, HF's clinical application is hampered by its limited water solubility, short $t_{1/2}$, and considerable non-target toxicity. Thus, designing a targeted nano-delivery system could offer a more precise and cutting-edge therapeutic choice, potentially overcoming these limitations. The comprehensive synthesis process of the HA-M@P@HF NPs is detailed in Scheme 1A.

At first, we employed an orthogonal experimental design so as to obtain the optimal EE of HA-M@P@HF NPs. The layout of the orthogonal test and its results following the L9(4^3) matrix are indicated in Fig. 2C and Table S3. Tables S4 and S5 indicate the detailed analysis of the orthogonal experiment, where a higher extreme difference (R_j) value signifies a more significant impact of the corresponding factor. For instance, in the encapsulation analysis, the R_j values for factors like PVA concentration (%, m/V) (A), PLGA/HF mass ratio (m/m) (B), W/O (V/V) (C), and rotation speed (rpm) (D) were 9.54, 2.36, 5.89, and 2.58, respectively, implying that the impact order on EE was A > C > D > B. Accordingly, the most favorable levels for each factor were identified as A_2-B_1-C_2-D_3. Consequently, the optimal conditions were deduced as 1% PVA, 5:1 PLGA-HF ratio, 10:1 W/O ratio, and a rotation speed of 1,200 rpm. Under these conditions, the EE reached 71.07% (Table S5). TEM images of the optimized P@HF NPs revealed their spherical morphology (Fig. 2D). To visualize the fusion of RBCm and Møm in varying proportions, we used DiI and DiO dyes to label RBCm and Møm, respectively. This process enabled observation of the hybridization, where a distinct yellow fluorescence indicated successful fusion in the NPs coated with M (Fig. 2E). Moreover, we discovered the most effective fusion rate at the 1:1 ratio of RBCm to Møm. The UV-vis spectra directly revealed characteristic absorption peaks of the M at wavelengths of 270, 414, 540, and 576 nm (Fig. 2F), due to the presence of both RBCm and Møm. Flow cytometry analysis demonstrated that the M (1:1) efficiently maintained the targeted uptake capability of Møm in activated macrophages, with approximately 1.6-fold the targeting efficiency of RBCm alone (Figs. 2G and S2A). Flow cytometry was then used to optimize the ratio of the targeted molecule HA to the carrier PLGA. A HA-PLGA ratio of 1:4 showed a 1.3-fold increase in targeting ability compared to a 1:8 ratio. However, further increasing this ratio to 1:2 did not enhance the targeting efficiency (Figs. 2H and S2B). Additionally, TEM images revealed that HA-M@P@HF NPs exhibited a core-shell structure, with P@HF NPs forming the core and the M membrane creating the shell (Fig. 2I).

DLS measurements showed the potential of approximately −21.2 mV for M@P@HF NPs, a reflection of the negative charge of the membrane. After modification with positive HA, the potential of HA-M@P@HF NPs was increased to −16.3 mV (Fig. 2J). FT-IR indicated a shift in the carboxylic O—H end group peak and C=C peak of PLGA NPs from 3,354 cm^{-1} and 1,656 cm^{-1} (Fig. S2C) to 3,336 cm^{-1} and 1,666 cm^{-1} of P@HF NPs, respectively (Fig. 2K), indicating HF

was encapsulated in the PLGA NPs. UV-vis analyses revealed that both P@HF and HA-M@P@HF NPs displayed HF's characteristic peak at 242 nm (Fig. 2L), further evidencing successful NP formulation. The hydrodynamic diameter of the HA-M@P@HF NPs was measured at approximately 163 nm (Fig. 2M), a size conducive to prolonged blood $t_{1/2}$ in NP delivery systems. Stability assessments indicated that HA-M@P@HF NPs maintained a consistent size over three days of storage at room temperature (Fig. S2D), demonstrating their favorable stability characteristics.

3.3. Characterization and cellular uptake of M-modified NPs

The SDS-PAGE analysis of HA-M@P@HF NPs demonstrated effective retention of key proteins derived from RBCm and Møm, as seen in the protein patterns of the NPs (Fig. 3A). Upon detection of specific protein markers, it was noted that CD47, an immunomodulatory protein from RBCm known for its role in macrophage inhibition, and CD11b, a protein predominantly expressed on macrophages, were both distinctly presented in the protein profiles of HA-M@P@HF NPs (Fig. 3B). These findings conclusively suggested that the natural cell membranes were successfully adsorbed onto the NPs, preserving their inherent biofunction.

As illustrated in Fig. 3C, activated macrophages and HFLS-RA displayed a notably higher red fluorescence intensity (FI) compared to intact macrophages and HFLS. This intensity was significantly reduced in activated macrophages and HFLS-RA pretreated with 500 μg/mL HA before incubation with NPs. Interestingly, there was no discernible difference in uptake efficiency between macrophages, HFLS, and HUVEC treated with HA-M@P@HF NPs, and those treated with P@HF NPs. These observations confirmed the dual-targeting capability of HA-M@P@HF NPs, particularly towards activated macrophages and HFLS-RA with a high affinity for the HA receptor. To further explore the cellular entry mechanism of these nanomaterials, inhibitors like 2-DG (an energy inhibitor), β-CD (inhibiting caveolae-mediated endocytosis), Colch (hindering macropinocytosis-mediated endocytosis), and chloroquine (blocking clathrin-mediated endocytosis) were employed. As depicted in Figs. S3A and B, the uptake efficiency of HA-M@P@HF NPs by activated macrophages was notably reduced in the presence of 2-DG, β-CD, and Colch. These findings suggested that the uptake of HA-M@P@HF NPs involved energy and predominantly entered cells through caveolae-mediated endocytosis and macropinocytosis, pathways known for circumventing lysosomal degradation. Next, the co-localization of HA-M@P@HF NPs within lysosome at different time points was performed to further elucidate their cellular uptake. As depicted in Figs. S3C and D, after 4 h of incubation, the fluorescence signal from the NPs was observed both in the cytoplasm and the nuclei of the cells. These findings suggested that the NPs could partially bypass lysosomal subcellular compartments, a crucial feature for reducing potential drug degradation by lysosomal enzymes.

Investigating the release profile of HA-M@P@HF NPs in acidic conditions mimicking joint inflammation revealed pH-responsive behavior. The release assay showed that approximately 58.2% of HF was released from the NPs over 72 h at pH 5.4, compared to about 44.3% at pH 7.4 (Fig. 3D). To deeply explore the drug release dynamics from HA-M@P@HF NPs, various mathematical models were applied, including zero-order kinetics, first-order kinetics, the Riger-Peppas model, the Higuchi model, and the Weibull model, to fit the *in vitro* release data. The best fit, determined by the highest R^2 coefficient, was found with the Weibull model for both pH 5.4 (Fig. 3E) and 7.4 (Fig. 3F) conditions, suggesting that the NPs exhibited sustained-release characteristics and followed Fickian diffusion as their primary release mechanism. The release process of these NPs was influenced by drug diffusion, matrix erosion, and
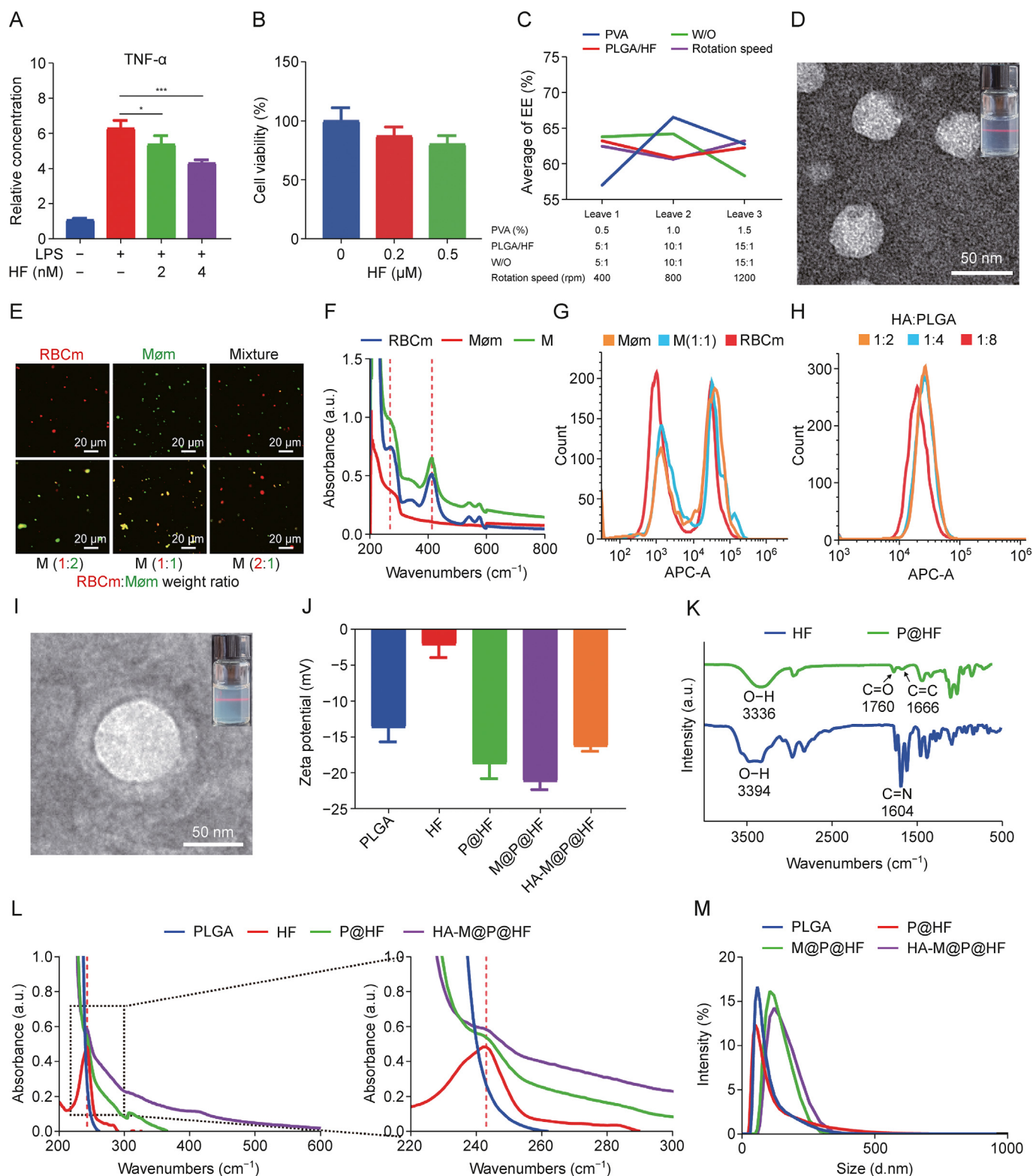
Fig. 2. Preparation and characterization of hyaluronic acid (HA)-modified hybrid membrane (M)-camouflaged poly lactic-*co*-glycolic acid (PLGA) loaded halofuginone hydrobromide (HF) nanoparticles (NPs) (HA-M@P@HF NPs). (A) *In vitro* inflammatory factor tumor necrosis factor-α (TNF-α) of macrophages after HF (2 and 4 nM) treatment. (B) Cell viability of human fibroblast-like synoviocytes-rheumatoid arthritis (HFLS-RA) following incubation with HF (0.2 and 0.5 μM) for 48 h. (C) Orthogonal experimental design and statistical analysis. (D) Transmission electron microscope (TEM) image of P@HF NPs (inset: image of P@HF NPs solution). (E) Fluorescent images of red blood cell membrane (RBCm) and macrophage membrane (Møm) mixture, and M (red for RBCm and green for Møm). (F) Ultraviolet-visible spectroscopy (UV-vis) of RBCm, Møm, and M. (G) Flow cytometry profiles of Møm@P@chlorin e6 (Ce6), M@P@Ce6, and RBCm@P@Ce6 uptake in activated macrophages. (H) Flow cytometry profiles of activated macrophage uptake achieved by HA-M@P@Ce6 loaded with different proportions of targeted molecule HA. (I) TEM image of HA-M@P@HF NPs (inset: image of HA-M@P@HF NPs solution). (J) Potential measurement of different NPs. (K) Fourier transform infrared spectroscopy (FT-IR) analysis of HF and P@HF. (L) UV-vis absorption spectra of HF, PLGA, P@HF, and HA-M@P@HF NPs. (M) Hydrodynamic size distribution of various NPs. LPS: lipopolysaccharide; EE: entrapment efficiency; PVA: polyvinyl alcohol; W/O: water-to-oil ratio; APC-A: a allophycocyanin-area.
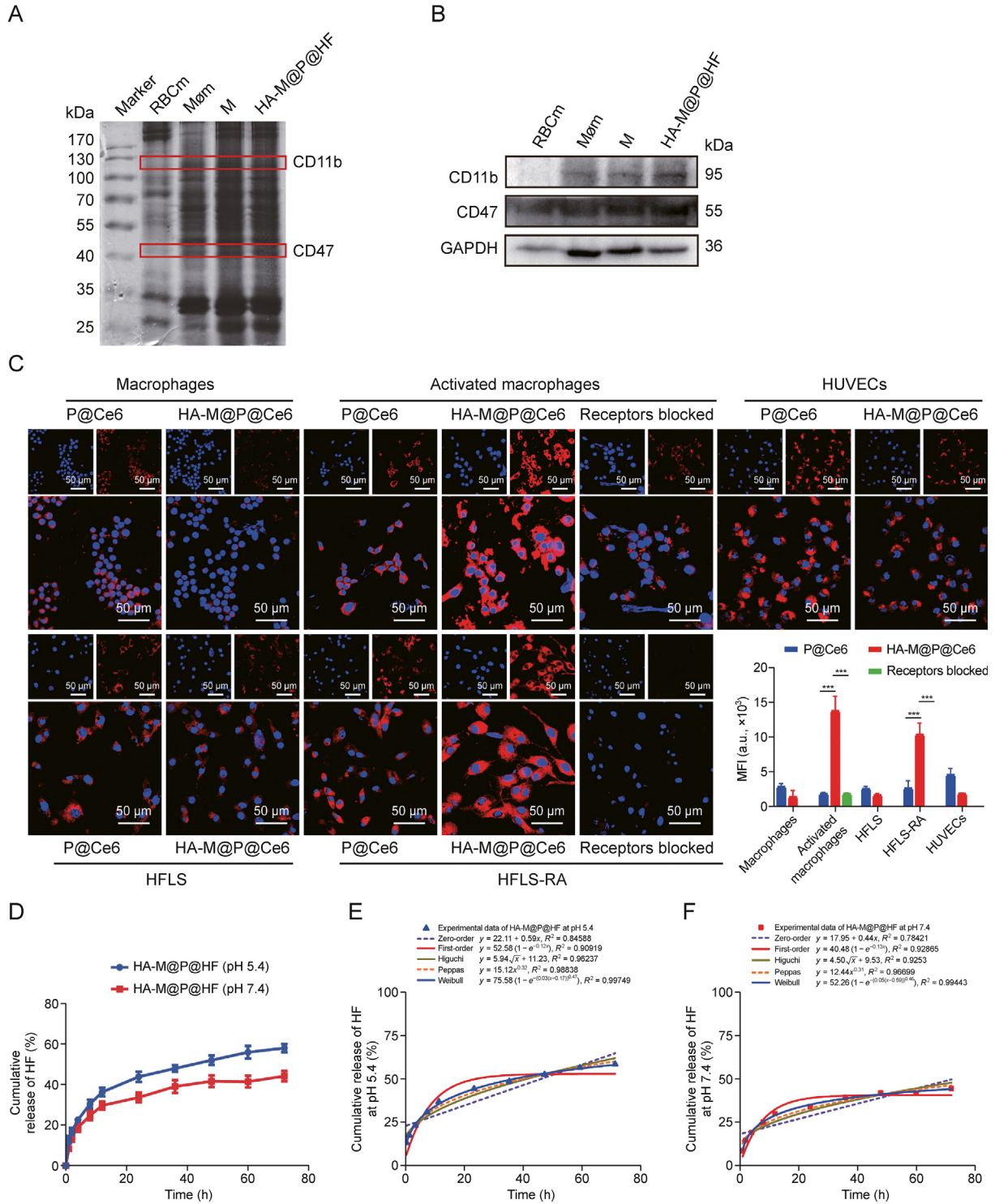
Fig. 3. Function and cellular uptake of hybrid membrane (M). (A) Sodium dodecyl sulfate-polyacrylamide gel electrophoresis (SDS-PAGE) analysis of the membrane proteins of marker, red blood cell membrane (RBCm), macrophage membrane (Møm), M, and hyaluronic acid (HA)-modified hybrid membrane (M)-camouflaged poly lactic-co-glycolic acid (PLGA) loaded halofuginone hydrobromide (HF) nanoparticles (NPs) (HA-M@P@HF NPs). (B) Detection of CD11b, CD47, and glyceraldehyde-3-phosphate dehydrogenase (GAPDH) in HA-M@P@HF NPs. (C) Fluorescent images of P@chlorin e6 (Ce6) and HA-M@P@Ce6 uptake in RAW264.7 cells, activated macrophages, human fibroblast-like synoviocytes (HFLS), HFLS-rheumatoid arthritis (RA), and human umbilical vein endothelial cell (HUVEC) for 4 h. (D) Cumulative release of HF from HA-M@P@HF NPs at pH 5.4 and 7.4. (E, F) Release kinetics of HA-M@P@HF NPs and various mathematical models of release mechanisms (i.e., zero-order model, first-order model, Higuchi model, Peppas model, and Weibull model) at pH 5.4 (E) and 7.4 (F). Data are presented as mean $\pm$ standard deviation ($n = 3$). ***$P < 0.001$. MFI: mean fluorescence intensity.

material degradation, with diffusion being the predominant factor. The strong affinity between HF and the PLGA matrix resulted in slow drug diffusion and sustained release. While the pH did not change the fundamental mechanism of NPs release, it did facilitate targeted drug delivery in acidic, inflammatory environments, thereby enabling precise treatment modulation at RA lesion sites.

3.4. Regulation of the immune-inflammation by HA-M@P@HF NPs

Macrophages are key players in both innate and adaptive immunity in nearly all tissues. Their ability to detect environmental changes and adapt their behavior is known as phenotypic plasticity, often referred to as M1/M2 macrophage polarization. This process involves changes in surface marker expression, factor production, and biological activity execution. Normally, macrophages maintain a dynamic balance in their phenotype, adjusting their functions in response to environmental shifts to sustain tissue homeostasis.

However, in the context of RA, there is a predominant shift towards the M1 phenotype from M2 macrophages, resulting in excess production of ROS and pro-inflammatory mediators like IL-6 and TNF-α, thus disrupting the immunoinflammatory homeostasis. Morphological observations revealed the round shape for typically undifferentiated macrophages. After stimulation with LPS, these cells become flat and elliptical, exhibiting an irregular morphology. Intriguingly, treatment with HA-M@P@HF NPs induced a shift back towards a more rounded macrophage form (Fig. 4A). This morphological change suggested the potential of NPs to modulate
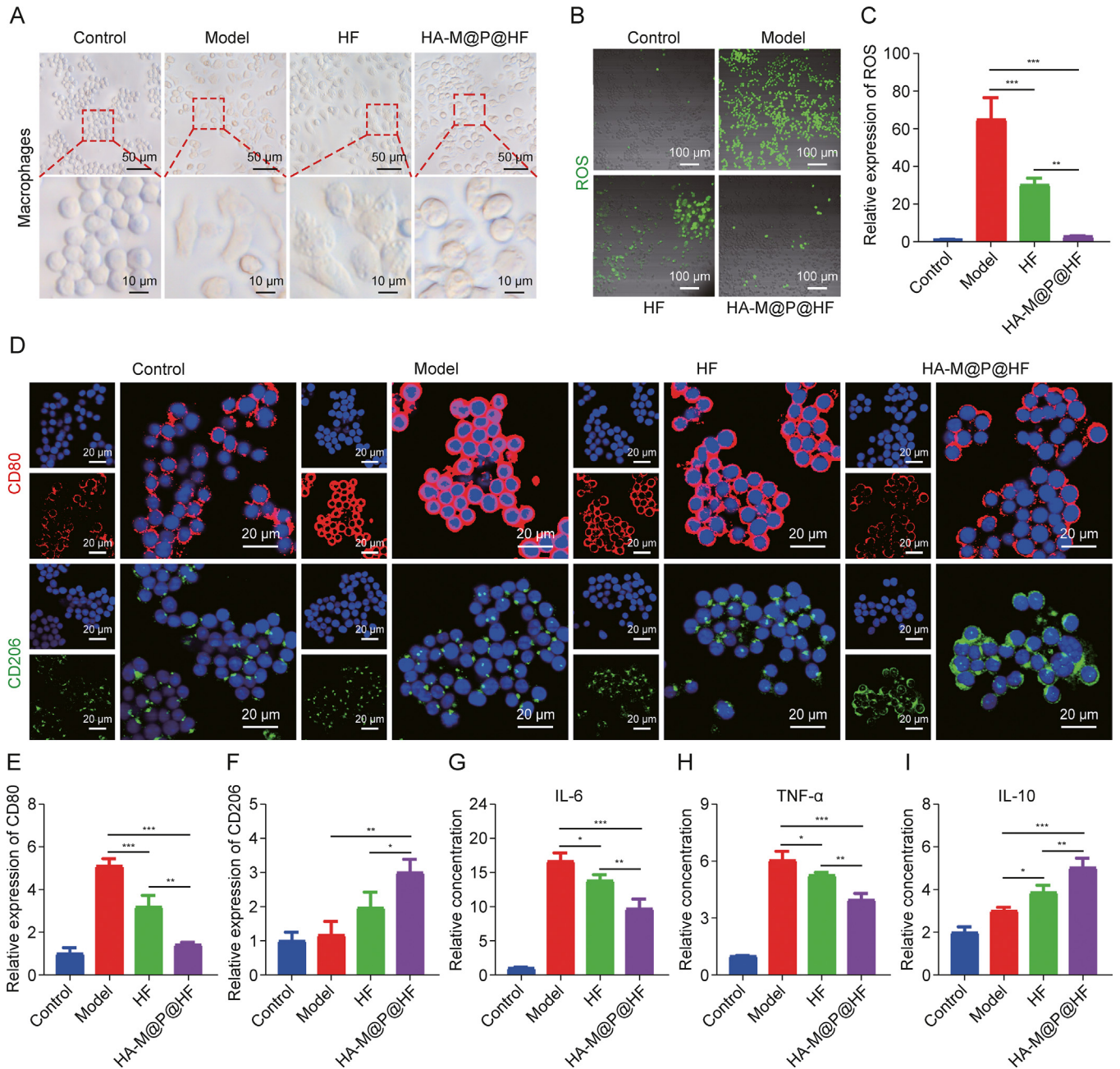

Fig. 4. The effect and mechanism of hyaluronic acid (HA)-modified hybrid membrane (M)-camouflaged poly lactic-*co*-glycolic acid (PLGA) loaded halofuginone hydrobromide (HF) nanoparticles (NPs) (HA-M@P@HF NPs) on the immune-inflammation of macrophages. (A) Morphology of macrophages treated with different drugs for 24 h at the concentration of 2 nM HF. (B, C) Representative fluorescence images (B) and quantitation (C) of reactive oxygen species (ROS) levels in cells incubated with different treatments. (D–F) Immuno-fluorescence staining (D), and quantitative analysis of CD80 (M1 biomarker, red) (E), and CD206 (M2 biomarker, green) (F) in macrophages with different treatments. (G–I) Enzyme-linked immunosorbent assay (ELISA) assay of interleukin-6 (IL-6) (G), tumor necrosis factor-α (TNF-α) (H), and IL-10 (I). Data are presented as mean $\pm$ standard deviation ($n = 3$). $^{*}P < 0.05$, $^{**}P < 0.01$, and $^{***}P < 0.001$. FI: fluorescence intensity.

macrophage phenotype and possibly restore the equilibrium within the macrophage microenvironment. Then, fluorescein probe was used to assess the effects of various NPs on intracellular ROS levels. As we expected, activated macrophages stimulated with LPS showed intense green fluorescence, an indication of elevated ROS levels. In turn, this effect was compromised by HA-M@P@HF NPs pretreatment (Figs. 4B and C). To evaluate the NPs' impact on macrophage repolarization, the phenotypic markers of the cells were analyzed through immunofluorescence staining. CD80, a biomarker for M1 macrophages, showed decreased expression, whereas CD206, indicative of M2 macrophages, became more prominent post-NPs treatment (Figs. 4D−F). This suggests an effective transition of macrophages from the M1 to the M2 phenotype. Additionally, the levels of macrophage biomarkers, including IL-6, TNF-α (M1 markers), and IL-10 (M2 marker), were quantified using ELISA. The results indicated that NPs notably reduced the levels of IL-6 and TNF-α of cells (Figs. 4G and H), while upregulating IL-10 (Fig. 4I). These findings suggest that NPs can modulate macrophage polarization, thereby exerting anti-inflammatory and immunomodulatory effects and influencing the expression of inflammatory cytokines.

3.5. Increased apoptosis rate of HFLS-RA treated with HA-M@P@HF NPs

Initially, we noted that HFLS-RA exhibited signs of apoptosis, such as reduced volume and cytoplasmic condensation, following treatment with 0.2 μM HF and HA-M@P@HF NPs (Fig. 5A). Cell cycle analyses of HFLS-RA by using flow cytometry exhibited that HF and HA-M@P@HF NPs treatment induced 2.43-fold and 3.56-fold increase in the proportion of cells in the G2/M phase, respectively. This suggests that the NPs can impede cell proliferation by inducing a G2 phase arrest (Figs. 5B and C). Additionally, G2/M phase proteins, P53 and P21, were upregulated by approximately 2.08-fold and 2.23-fold, respectively, following with HA-M@P@HF NPs treatment (Figs. 5D and E). These findings indicate that HA-M@P@HF NPs effectively inhibit cell proliferation by blocking the G2/M phase via the activation of the P53/P21 pathway. In addition, fluorescence-activated cell sorting (FACS) assay showed that late and early apoptosis rates of HFLS-RA treated with HA-M@P@HF NPs were 35.37% (Q2) and 2.91% (Q3), respectively. The apoptosis rate was significantly greater than that of PBS-treated cells (Figs. 5F and G). Western blot analyses demonstrated that HA-M@P@HF NPs markedly increased the expression of BAX and decreased Bcl-2 levels in HFLS-RA (Figs. 5H and I). The results indicate that HA-M@P@HF NPs significantly promote apoptosis of HFLS-RA. Additionally, the cell viability of HFLS-RA cultured for 48 h in an M1 macrophage inflammatory environment was higher than that of those under conventional culture; however, this enhanced cell viability was significantly mitigated when NPs were introduced into the inflammatory environment. Our data suggest that NPs may suppress abnormal proliferation of HFLS-RA by modulating macrophage-induced inflammation and inhibiting cell viability of HFLS-RA (Figs. 5J and K), which requires further investigation of the interaction proteins between macrophage polarization and HFLS-RA apoptosis.

3.6. Pharmacokinetics and biodistribution of HA-M@P@HF NPs in inflamed joints of AIA rats

To assess the effectiveness of HA-M@P@HF NPs in treating RA, Ce6 labeled NPs was used to perform pharmacokinetic study in AIA rats. Fig. 6A indicated a significant increase in the circulation $t_{1/2}$ of HA-M@P@Ce6 compared to P@Ce6. UPLC-MS/MS was then employed to measure the actual blood drug concentration and $t_{1/2}$ of these NPs (Fig. S4A). The $t_{1/2}$ of HF, P@HF, and HA-M@P@HF NPs were determined to be 2.55, 3.24, and 5.02 h, respectively (Fig. 6B). This finding underscores the efficacy of the M in prolonging the bloodstream circulation of the nanomaterials. Building on these promising findings, AIA rats were intravenously administered P@Ce6 or HA-M@P@Ce6 NPs. The arthritis-targeting capabilities of these NPs were then meticulously evaluated by fluorescence imaging of the arthritic hind paws at various time points (Figs. 6C and D). Following the administration of P@Ce6, only a faint fluorescence signal was detected in the arthritic paws, likely due to rapid metabolism and lack of specific targeting. In contrast, the arthritic paws showed strong fluorescence signal after HA-M@P@Ce6 administration, due to the efficient targeting of NPs. Additionally, the metabolic pathways of these nanomaterials were analyzed by performing *ex vivo* fluorescence imaging and UPLC-MS/MS analysis of major organs. Fluorescence imaging indicated that HF, P@HF, and HA-M@P@HF NPs were primarily metabolized through the kidneys and liver (Figs. S4B and C). Subsequent UPLC-MS/MS analysis demonstrated a significantly higher concentration of HF in the joints of AIA rats treated with HA-M@P@HF NPs, 48 h post intravenous administration. The drug concentration in arthritic tissues with HA-M@P@HF NPs administration was about 1.47-fold higher and approximately 5.39-fold higher than that of P@HF NPs and free HF, respectively (Fig. 6E). These findings illustrate the targeted accumulation of HA-M@P@HF NPs at arthritic sites. Collectively, these results suggest that HA-M@P@HF NPs with prolonged circulation life can accumulate at arthritic sites to enhance the specific therapeutic efficacy of drugs.

3.7. Therapeutic efficacy of HA-M@P@HF NPs in AIA rats

In our study, the therapeutic effects of HA-M@P@HF NPs were assessed in AIA rats. Following the injection of CFA, AIA rats displayed noticeable symptoms of arthritis characterized by swelling and erythema in the paws as well as rheumatoid nodules, skin redness, and ulceration in the tails on day 9 (Fig. S5A). Eventually, these rats all developed severe arthritis. In stark contrast, rats treated with HA-M@P@HF NPs exhibited significantly lower levels of arthritis (Fig. S5B), evidenced by the paw swelling volume (Fig. 7A) and arthritis severity scores (Fig. 7B), closely resembling those of normal control rats. Histological examination of the joints further highlighted the therapeutic impact. H&E stained sections indicated significant immune cell infiltration (indicated by a star) and angiogenesis (red arrow) in the synovium of AIA rats. Similar findings were observed in other treatment groups. However, the HA-M@P@HF NPs group demonstrated markedly smooth joint surfaces, reduced immune cell infiltration, and less angiogenesis (Figs. 7C and D). This reduction in synovial inflammation, crucial in perpetuating RA by attracting and activating immune cells and persistently damaging joint tissues [33], underscores the potential of HA-M@P@HF NPs for effective anti-arthritic treatment. In Masson's trichrome-stained joint sections, irregularly distributed collagen fibers with high density in the AIA group indicated tissue fibrosis by forming a network-like structure. However, the group treated with HA-M@P@HF NPs showed a notable reduction in collagen fibers and normal tissue-like architecture (Figs. 7E and F). Additionally, SO-FG staining demonstrated significant cartilage repair in the HF-treated group, with HA-M@P@HF NPs-treated rats exhibiting complete and normal cartilage structure, as opposed to the extensive cartilage damage (black arrow) seen in the AIA group (Figs. 7G and H). CT scan was performed to assess bone health. As illustrated in Figs. 7I and J, the AIA group considerably reduced bone density and indicated extensive bone damage compared to healthy control. In contrast, rats treated with
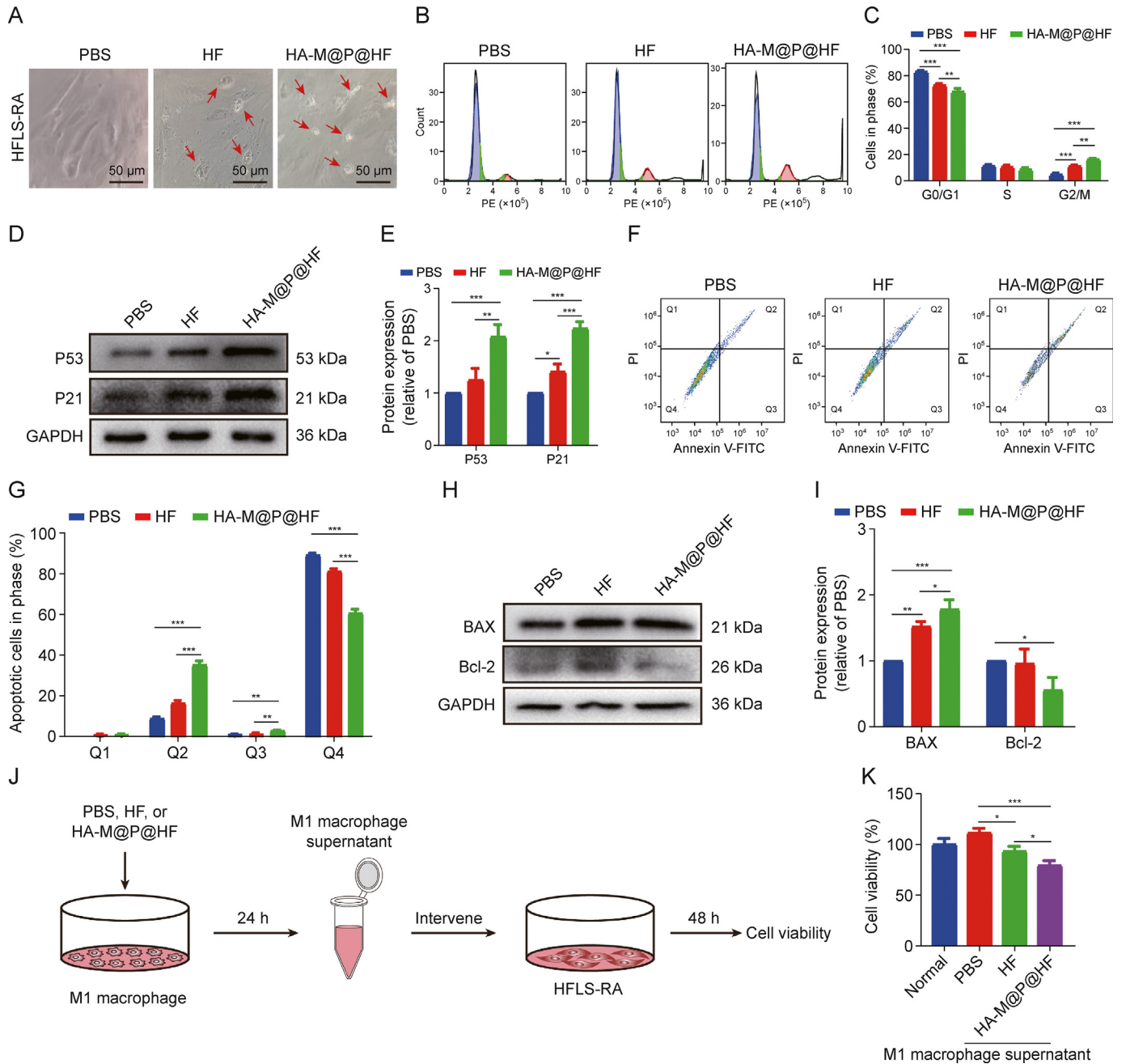
Fig. 5. *In vitro* anti-arthritic effects and mechanism of hyaluronic acid (HA)-modified hybrid membrane (M)-camouflaged poly lactic-*co*-glycolic acid (PLGA) loaded halofuginone hydrobromide (HF) nanoparticles (NPs) (HA-M@P@HF NPs). (A) Morphological images of human fibroblast-like synoviocytes-rheumatoid arthritis (HFLS-RA) with different treatments for 48 h. The red arrows indicate apoptotic cells. (B, C) Flow cytometry images (B) and quantitative analysis (C) of cell cycle assay of HFLS-RA with different treatments by flow cytometry. (D, E) Western blotting assay (D) and quantitative analysis (E) of P53 and P21 levels with different treatments. (F, G) Apoptosis detection (F) and quantitation (G) after various treatments by flow cytometry. Q1–Q4 indicate necrosis rate, late apoptosis rate, early apoptosis rate, and non-apoptotic rate, respectively. (H, I) Western blot images (H) and quantitative analysis (I) of Bcl-2-associated X protein (BAX) and Bcl-2 levels with different treatments. (J) Intervention process of M1 macrophage inflammatory supernatant on HFLS-RA. (K) The effect of M1 macrophage inflammatory environment on the cell viability of HFLS-RA. Phosphate-buffered saline (PBS) was used as the negative control. Data are presented as mean ± standard deviation ($n = 3$). $^*P < 0.05$, $^{**}P < 0.01$, and $^{***}P < 0.001$. PE: phycoerythrin; GAPDH: glyceraldehyde-3-phosphate dehydrogenase; PI: propidium iodide; FITC: fluorescein isothiocyanate.

either free HF or HA-M@P@HF NPs showed noticeable improvement in bone density and less bone loss, compared to the AIA group. Notably, the HA-M@P@HF NPs group displayed intact bone tissue and enhanced bone density, closely resembling the structure of healthy bone. This improvement can be attributed to the macrophage homeostasis in the microenvironment, potentially leading to a reduction in osteoclasts, which are known to resorb and damage bone [34–36]. These findings demonstrate
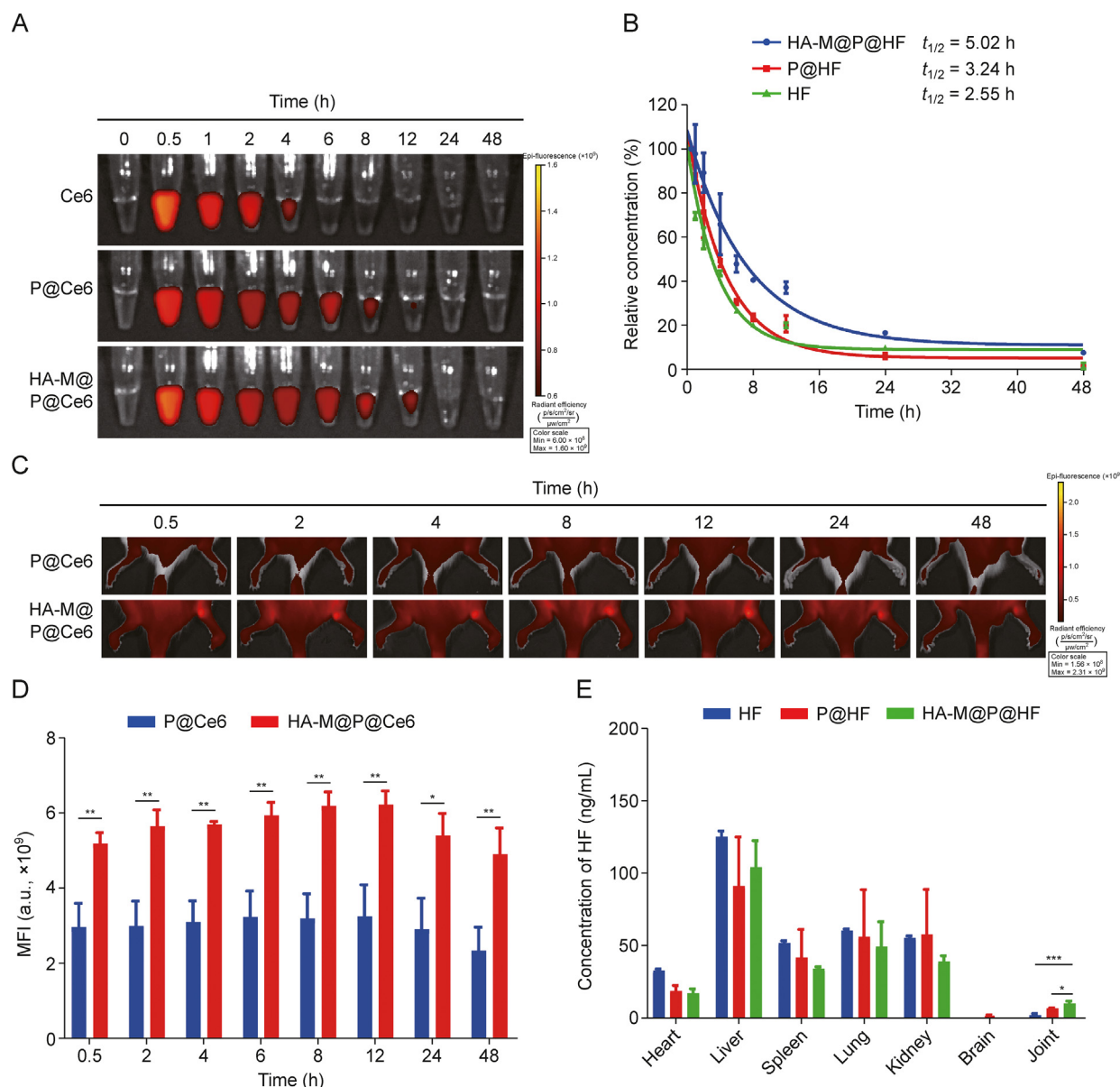
Fig. 6. Pharmacokinetic and biodistribution of hyaluronic acid (HA)-modified hybrid membrane (M)-camouflaged poly lactic-*co*-glycolic acid (PLGA) loaded halofuginone hydrobromide (HF) nanoparticles (NPs) (HA-M@P@HF NPs) in adjuvant-induced arthritis (AIA) rats. (A) The fluorescence images of chlorin e6 (Ce6), P@Ce6, and HA-M@P@Ce6 NPs in the blood of rats at different time points. (B) Pharmacokinetic curves of HF, P@HF, and HA-M@P@HF NPs over time determined by ultra-performance liquid chromatography tandem mass spectrometry (UPLC-MS/MS). (C, D) Fluorescent distribution (C) and quantification (D) in affected joints. (E) Determination of drug concentration in major organs after 48 h post-injection by UPLC-MS/MS. Data are presented as mean ± standard deviation ($n = 3$). $^*P < 0.05$, $^{**}P < 0.01$, and $^{***}P < 0.001$. $t_{1/2}$: half-life; MFI: mean fluorescence intensity.

that HA-M@P@HF NPs can effectively target RA sites and provide superior therapeutic benefits for RA management.

3.8. Inhibition of synovial hyperplasia and protection of bone destruction by HA-M@P@HF NPs via regulating immune inflammation in the RA joints

Several methods were used to assess the regulation of ROS, the M1-to-M2 macrophage phenotype transition, and the presence of HFLS-RA *in vivo*. Immunofluorescence staining demonstrated substantial decrease in ROS levels post-treatment with HF and HA-

M@P@HF NPs about 51.06% and 80.51%, respectively, compared to the AIA group. Notably, HA-M@P@HF NPs treatment effectively reversed ROS levels to near-normal range (Figs. 8A and B). Furthermore, treatments with both HF and HA-M@P@HF NPs led to a reduction in CD80 (an M1 biomarker) and an increase in CD206 (an M2 biomarker) expression (Fig. 8C). The HA-M@P@HF NPs treatment particularly restored the CD80-to-CD206 ratio to levels under normal conditions (Fig. 8D), indicating an *in vivo* repolarization of macrophages from the pro-inflammatory M1 to anti-inflammatory M2 phenotype. Serum cytokine analysis showed that both HF and HA-M@P@HF NPs decreased the levels of TNF-α
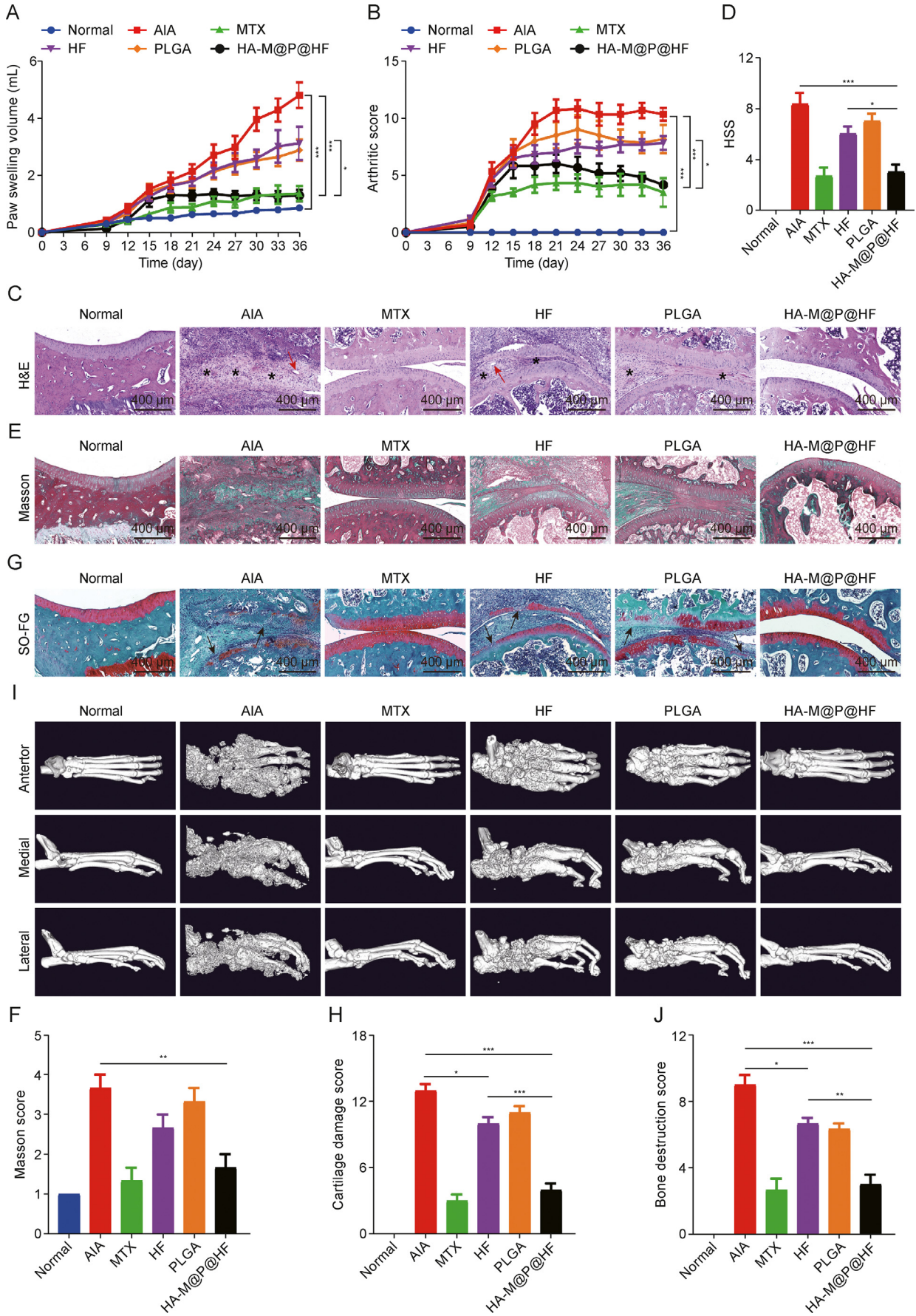
and IL-6 (biomarkers of M1 type) and increased IL-10 (biomarker of M2 type). The effect was mostly pronounced with HA-M@P@HF NPs, underscoring their significant role in facilitating the M1-to-M2 phenotype transition *in vivo* (Fig. 8E). Immunohistochemical analysis targeting Ki67 (a biomarker for HFLS-RA proliferation and invasion) and CD44 (a biomarker for HFLS-RA) revealed significant pathological changes in AIA rats. The invasive ability marked by Ki67 was about 2.52-fold higher than that of normal synovial fibroblasts (Figs. 8F and G), while the expression of CD44 was approximately 3.21-fold higher in AIA rats than that of normal rats (Figs. 8H and I). However, these effects were notably mitigated by treatment with HF or HA-M@P@HF NPs. Notably, the inhibitory impact of HA-M@P@HF NPs on HFLS-RA proliferation and invasion surpassed that of the HF group, closely aligning with the conditions found in healthy synovium. TUNEL staining showed the most potent apoptosis-inducing effect of HA-M@P@HF NPs on HFLS-RA, evidenced by the highest FI in synovial sections (Figs. 8J and K). Moreover, TRAP staining indicated an abundance of osteoclasts (dark red spots) in the joints of AIA rats compared to healthy controls. Both HF and HA-M@P@HF NPs treatments significantly reduced osteoclast number, with HA-M@P@HF NPs achieving levels comparable to those in healthy rats (Figs. 8L and M). These findings underscore the therapeutic potential of HA-M@P@HF NPs in inducing apoptosis in HFLS-RA, curbing synovial hyperplasia, and preserving joint bone tissue in AIA rats.

Traditionally, clinical treatments for arthritis and synovial hyperplasia have primarily focused on halting disease progression and mitigating inflammation. However, up to half of newly used DMARD patients terminate treatment due to the low efficacy or adverse side effects, and approximately 20%−30% of patients do not respond to existing therapies, underscoring the critical need for more multifaceted treatment approaches [37]. Previous research has explored targeting macrophage inflammation or synovial proliferation as potential nanomedicine strategies, yet these approaches have faced challenges like limited specificity, singular action, and high costs (Table 1) [38−42]. Therefore, we developed dual-targeted HF nanocomplexes for efficient and precise delivery to macrophages and HFLS-RA. Our findings demonstrated that HA-M@P@HF NPs effectively restored immune-inflammatory homeostasis *in vivo* by diminishing ROS levels and facilitating the repolarization of M1 to M2 macrophages. On the other hand, HA-M@P@HF NPs promoted the apoptosis of aberrantly proliferative synovial cells and inhibited synovial hyperplasia. This dual action significantly reduced osteoclast numbers, thereby protecting AIA rats from bone damage and offering a promising therapeutic avenue for RA. Consequently, HA-M@P@HF NPs showed potential as a novel treatment modality for RA.

3.9. Safety and clinical application prospects of HA-M@P@HF NPs

The biocompatibility and biosafety of HA-M@P@HF NPs were thoroughly evaluated to ascertain their clinical applicability. Initial *in vitro* tests on the interaction of HA-M@P@HF NPs with PLT showed an extremely low risk of PLT aggregation (Fig. S6A).

Additionally, hemolysis assays demonstrated that all RBC hemolysis rates were under 5% when exposed to PLGA, P@HF, and HA-M@P@HF NPs (Fig. S6B). Furthermore, RBC morphology remained unchanged following exposure to 40 μg/mL of HA-M@P@HF NPs (Fig. S6C). The cytotoxicity of HA-M@P@HF NPs was also evaluated using RAW264.7, HFLS, VSMC, HUVEC, HL7702, HK2, and H9C2 (Fig. S6D). The negligible cytotoxicity for these representative cell lines, indicated the high biocompatibility of HA-M@P@HF NPs.

Comprehensive hematological, biochemical, and histological analyses were conducted to assess the safety profile of HA-M@P@HF NPs in AIA rats. Hematological parameters, which were previously abnormal in AIA rats, normalized to levels comparable to the healthy control group following treatment with HA-M@P@HF NPs. All measured parameters fell within healthy reference ranges (indicated by red dashed lines), demonstrating the safety of this nanomedicine (Figs. 9A−H). Notably, white blood cell (WBC) and PLT counts, indicators of bodily inflammation, were elevated in AIA rats but returned to normal levels post-treatment, indicating the NPs' anti-inflammatory efficacy *in vivo*. Considering that the liver and kidneys are primary organs for NPs clearance, liver function tests (including alanine transaminase (ALT) and aspartate aminotransferase (AST)) and renal function tests (including blood urea nitrogen (BUN) and creatinine (Cr)) were performed. Results showed that HA-M@P@HF NPs did not cause any significant alterations in liver or renal functions compared to the normal group (Figs. 9I−L). Histological examination also revealed no significant tissue damage in the major organs of rats treated with HA-M@P@HF NPs (Fig. 9M). These findings highlight a favorable *in vivo* biosafety profile for HA-M@P@HF NPs when intravenously administered to AIA rats, suggesting their suitability for therapeutic use.

An analysis of hematological parameters in 30 healthy volunteers and 30 patients with RA revealed notable differences in various blood indices. WBC count, a crucial component of the immune system involved in identifying and eliminating foreign substances, pathogens, and abnormal cells [43], was found to be significantly altered in RA patients (Fig. S7A). This includes changes in neutrophil (NEU) levels (Fig. S7B), monocyte (MONO) counts (Fig. S7C), and LYM numbers (Fig. S7D). In RA, NEUs often migrate into joint areas and can be activated by inflammatory cytokines. These activated NEUs then interact with HFLS-RA, contributing to the inflammatory response. Similarly, MONOs in the joint area can differentiate into various macrophage phenotypes, such as M1 or M2, depending on the stimuli and environmental factors, playing a pivotal role in the acute inflammatory phase of RA.

LYM in RA patients differentiate into critical immune cells such as B and T LYMs, which are integral to RA pathogenesis. Additionally, RA can lead to RBC aggregation, as evidenced by changes in hematocrit (HCT) (Fig. S7E) and anemia, indicated by altered hemoglobin (HGB) levels (Fig. S7F). There is also a risk of cardiovascular and cerebrovascular issues due to thrombocytosis, shown by variations in PLT (Fig. S7G) and PLT distribution width (PDW) (Fig. S7H). Although RA patients showed normal liver function

Fig. 7. Therapeutic efficacy of hyaluronic acid (HA)-modified hybrid membrane (M)-camouflaged poly lactic-*co*-glycolic acid (PLGA) loaded halofuginone hydrobromide (HF) nanoparticles (NPs) (HA-M@P@HF NPs) *in vivo*. (A, B) Paw swelling volume (A) and arthritis severity scores (B) in adjuvant-induced arthritis (AIA) rats injected with saline (normal), methotrexate (MTX), HF (0.25 mg/kg), PLGA, or HA-M@P@HF NPs (HF 0.25 mg/kg) ($n = 6$ per formulation). (C, D) Hematoxylin-eosin (H&E) staining (C) and histopathological synovial score (HSS) (D) of the synovial joints. The star means immune cell infiltration and the red arrow means angiogenesis. (E, F) Masson staining (E) and score (F) of the synovial joints. (G, H) Safranin O-fast green (SO-FG) staining (G) and cartilage damage score (H) of the ankle joints. The black arrow means cartilage damage. (I, J) Micro-computed tomography (CT) (I) and bone destruction score (J) of normal control, AIA rats, and different treatment groups. Data are presented as mean ± standard deviation ($n = 3$). $^{*}P < 0.05$, $^{**}P < 0.01$, and $^{***}P < 0.001$.
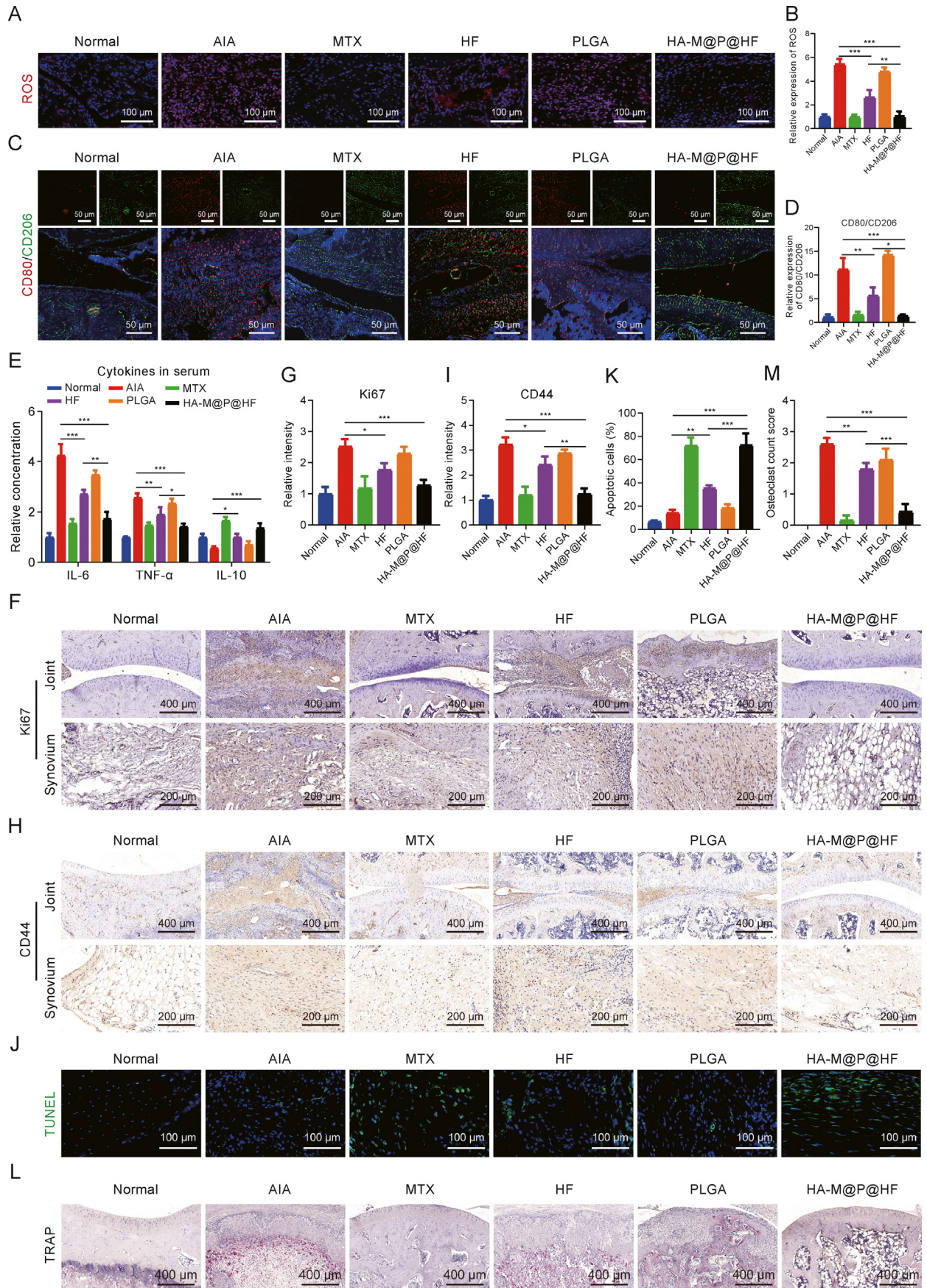
Table 1
Comparison of recovery after rheumatoid arthritis (RA) using different medicines.

Nanomedicines	*In vitro* dosage	*In vivo* dosage	Therapeutic effects	Advantages and disadvantages	Refs.
Macrophage-hitchhiking IL-10 pDNA delivery system	8 µg/well	150 µg/rat, intraperitoneal injection	Modulates RA microenvironment	Advantages: inducing the repolarization of macrophages and reducing the production of proinflammatory cytokines Disadvantages: not cost-effective	[38]
Mannose-modified azocalix[4]arene and ginsenoside Rb1	500 µM	15.5 mg/kg, intravenous injection	Macrophage polarization and anti-inflammatory	Advantages: simple synthesis, triple targeting (ELVIS targeting, macrophage-targeting, and hypoxia-targeted release) and triple therapy (ROS scavenging, macrophage polarization, and the anti-inflammatory effect) Disadvantages: high dosage of medication	[39]
Leonurine and catalase co-loaded nanoliposomal system	10 µM	10 mg/kg, intravenous injection	Remodeling the hostile RA microenvironment	Advantages: Synergistic effects of macrophage polarization, inflammation resolution, ROS scavenging, and hypoxia relief Disadvantages: single targeting	[40]
Iguratimod/PVA nanodrugs	40−320 µg/mL	3.3 mg/kg, oral administration	Inhibition of proliferation, migration, and invasion of synovial fibroblasts	Advantages: cost-effective Disadvantages: no targeting	[41]
PLGA-encapsulated metformin and indocyanine green	2 µg/mL	10 mg/kg, intraperitoneal injection	Anti-inflammation and polarization of macrophages.	Advantages: Enhances anti-inflammatory by incorporating photothermal therapy Disadvantages: weak specificity targeting.	[42]
HA-M@P@HF NPs	2 nM	0.25 mg/kg, intravenous injection	Regulation of immune inflammation and inhibition of synovial hyperplasia	Advantages: dual targeting (inflammatory macrophages and HFLS-RA targeting), effective therapy by regulating immune inflammation (macrophage repolarization, ROS scavenging, and anti-inflammatory) and inhibiting synovial hyperplasia (impeding HFLS-RA proliferation and promoting HFLS-RA apoptosis), safe, and cost-effective. Disadvantages: The interaction mechanism between inflammatory macrophages and HFLS-RA has not yet been fully elucidated.	This work

IL-10: interleukin-10; pDNA: plasmid DNA; RA: rheumatoid arthritis; ELVIS: extravasation through leaky vasculature and subsequent inflammatory cell-mediated sequestration; ROS: reactive oxygen species; PVA: polyvinyl alcohol; PLGA: poly lactic-*co*-glycolic acid; HA-M@P@HF NPs: hyaluronic acid (HA)-modified hybrid membrane (M)-camouflaged PLGA loaded halofuginone hydrobromide (HF) nanoparticles (NPs); HFLS: human fibroblast-like synoviocytes.

(Figs. S7I and J), but BUN (Fig. S7K), a renal function marker, often abnormally increased, possibly due to the renal filtration impairments caused by RA [44]. Additionally, there was no significant change in Cr (Fig. S7L). These observations were also mirrored in AIA rats, indicating that the model effectively replicates RA pathogenesis. The blood profiles of RA patients offer valuable insights for future research directions. Developing a reliable method for isolating immune cells from RA patient's peripheral blood could deeply investigate the interactions between NEUs, mononuclear macrophages, and synovial proliferation in the human body. Such research could greatly inform RA-targeted immunoregulation and anti-proliferation strategies, laying the groundwork for personalized treatment and advancing clinical practice in RA management.

Fig. 8. Hyaluronic acid (HA)-modified hybrid membrane (M)-camouflaged poly lactic-*co*-glycolic acid (PLGA) loaded halofuginone hydrobromide (HF) nanoparticles (NPs) (HA-M@P@HF NPs) alleviate rheumatoid arthritis (RA) by regulating immune-inflammation. (A, B) Immunofluorescence staining (A) and quantitative analysis (B) of reactive oxygen species (ROS) in synovium. (C, D) Immunofluorescence staining (C) and quantitative analysis (D) of CD80 (red) and CD206 (green) in the normal and inflamed joints after different treatments. (E) Enzyme-linked immunosorbent assay (ELISA) analysis of serum interleukin-6 (IL-6), tumor necrosis factor-α (TNF-α), and IL-10 levels after various treatments. (F, G) Immunohistochemical staining (F) and quantitation (G) of Ki67 in the normal and adjuvant-induced arthritis (AIA) rat paws after different treatments. (H, I) Immunohistochemical staining (H) and quantitation (I) of CD44 in the normal and inflamed joints after different treatments. (J, K) Immunofluorescence images (J) and quantitation (K) of the synovium stained with terminal deoxynucleotidyl transferase-mediated nick end labeling (TUNEL) assay kit. (L, M) Tartrate resistant acid phosphatase (TRAP) staining (L) and osteoclast count score (M) in the normal and arthritic paws. Data are presented as mean ± standard deviation ($n = 3$). $^*P < 0.05$, $^{**}P < 0.01$, and $^{***}P < 0.001$. MTX: methotrexate. FI: fluorescence intensity.
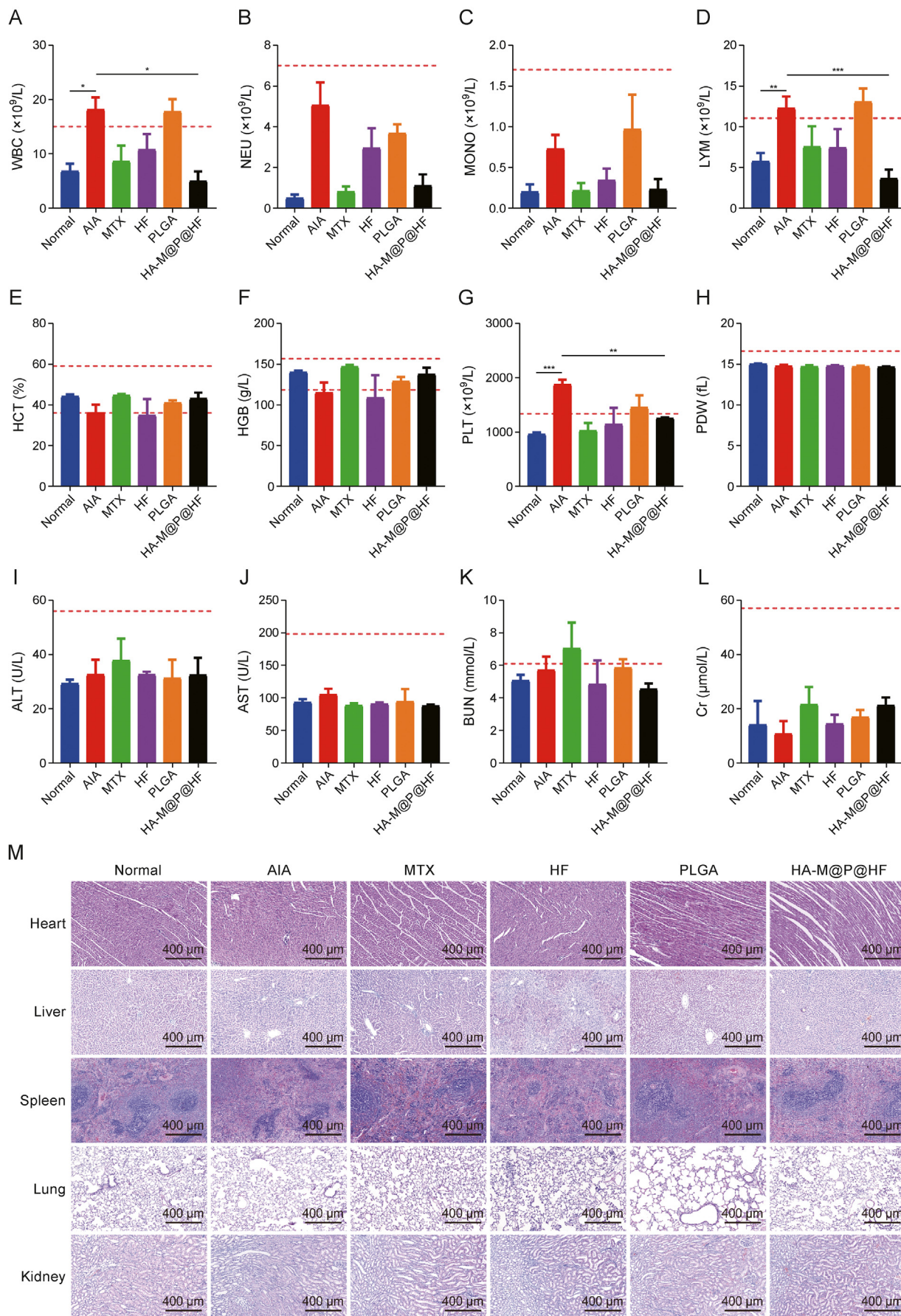
4. Conclusions

In conclusion, our developed HA-M@P@HF NPs complexes offered the dual-targeted anti-arthritic drug for more effective treatment of RA. These NPs synergistically suppressed immune inflammation as well as inhibited synovial hyperplasia in synovial joints. The HA-M@P@HF NPs not only restored immune-inflammatory balance by facilitating the polarization of macrophages from M1 to M2, but also addressed synovial hyperplasia by curtailing the proliferation of HFLS-RA and enhancing their apoptosis. Treatment with HA-M@P@HF NPs led to a reduction in osteoclast numbers, and therefore safeguarded cartilage and bone to ultimately protect inflamed joints from destruction. Furthermore, HA-M@P@HF NPs exhibited a prolonged circulation $t_{1/2}$, exceptional biocompatibility, and well-documented safety. Collectively, these attributes, in conjunction with the innovative therapeutic strategy they represent, pave the way for new and effective treatment for RA.

CRediT authorship contribution statement

Junping Zhu: Conceptualization, Data curation, Formal analysis, Methodology, Project administration, Writing − original draft, Writing − review & editing. **Ye Lin:** Conceptualization, Data curation, Formal analysis, Methodology, Project administration, Writing − original draft, Writing − review & editing. **Gejing Li:** Methodology, Software. **Yini He:** Methodology, Software. **Zhaoli Su:** Software, Visualization. **Yuanyuan Tang:** Software, Visualization. **Ye Zhang:** Software, Visualization. **Qian Xu:** Data curation. **Zhongliu Yao:** Data curation. **Hua Zhou:** Conceptualization, Funding acquisition, Resources, Supervision, Validation, Writing − review & editing. **Bin Liu:** Conceptualization, Funding acquisition, Resources, Supervision, Validation, Writing − review & editing. **Xiong Cai:** Conceptualization, Funding acquisition, Resources, Supervision, Validation, Writing − review & editing.

Declaration of competing interest

The authors declare that there are no conflicts of interest.

Acknowledgments

Appendix A. Supplementary data

Supplementary data to this article can be found online at https://doi.org/10.1016/j.jpha.2024.100981.

References

[1] A. Di Matteo, J.M. Bathon, P. Emery, Rheumatoid arthritis, Lancet 402 (2023) 2019−2033.
[2] Y. Ma, Z. Lu, B. Jia, et al., DNA origami as a nanomedicine for targeted rheumatoid arthritis therapy through reactive oxygen species and nitric oxide scavenging, ACS Nano 16 (2022) 12520−12531.
[3] E.M.L. Philippon, L.J.E. van Rooijen, F. Khodadust, et al., A novel 3D spheroid model of rheumatoid arthritis synovial tissue incorporating fibroblasts, endothelial cells, and macrophages, Front. Immunol. 14 (2023), 1188835.
[4] J. Tu, X. Wang, X. Gong, et al., Synovial macrophages in rheumatoid arthritis: The past, present, and future, Mediators Inflamm. 2020 (2020), 1583647.
[5] J. Zhu, J. Wei, Y. Lin, et al., Inhibition of IL-17 signaling in macrophages underlies the anti-arthritic effects of halofuginone hydrobromide: Network pharmacology, molecular docking, and experimental validation, BMC Complement. Med. Ther. 24 (2024), 105.
[6] J. Smolen, R.B. Landewé, P. Mease, et al., Efficacy and safety of certolizumab pegol plus methotrexate in active rheumatoid arthritis: The RAPID 2 study. A randomised controlled trial, Ann. Rheum. Dis. 68 (2009) 797−804.
[7] E. Berthet, M. De Rosa, P. Vorilhon, et al., AB1073 Exploration of the difficulties encountered by general practitioners with methotrexate and tnf-inhibitor treatment in common practice, Ann. Rheum. Dis. 75 (2016), 1268.
[8] R.A. Moura, J.E. Fonseca, JAK inhibitors and modulation of B cell immune responses in rheumatoid arthritis, Front. Med. 7 (2021), 607725.
[9] M.K. Park, J.S. Park, E.M. Park, et al., Halofuginone ameliorates autoimmune arthritis in mice by regulating the balance between Th17 and Treg cells and inhibiting osteoclastogenesis, Arthritis Rheumatol. 66 (2014) 1195−1207.
[10] S. Zeng, K. Wang, M. Huang, et al., Halofuginone inhibits TNF-α-induced the migration and proliferation of fibroblast-like synoviocytes from rheumatoid arthritis patients, Int. Immunopharmacol. 43 (2017) 187−194.
[11] J. Gill, A. Sharma, Prospects of halofuginone as an antiprotozoal drug scaffold, Drug Discov. Today 27 (2022) 2586−2592.
[12] K. Park, S. Skidmore, J. Hadar, et al., Injectable, long-acting PLGA formulations: Analyzing PLGA and understanding microparticle formation, J. Control. Release 304 (2019) 125−134.
[13] J. Fan, Y. Qin, C. Xiao, et al., Biomimetic PLGA-based nanocomplexes for improved tumor penetration to enhance chemo-photodynamic therapy against metastasis of TNBC, Mater. Today Adv. 16 (2022), 100289.
[14] J. Lu, X. Gao, S. Wang, et al., Advanced strategies to evade the mononuclear phagocyte system clearance of nanomaterials, Exploration (Beijing) 3 (2023), 20220045.
[15] D. Liu, A. Yang, Y. Li, et al., Targeted delivery of rosuvastatin enhances treatment of HHcy-induced atherosclerosis using macrophage membrane-coated nanoparticles, J. Pharm. Anal. 14 (2024), 100937.
[16] P. You, A. Mayier, H. Zhou, et al., Targeting and promoting atherosclerosis regression using hybrid membrane coated nanomaterials via alleviated inflammation and enhanced autophagy, Appl. Mater. Today 26 (2022), 101386.
[17] Y. Lin, O. Yi, M. Hu, et al., Multifunctional nanoparticles of sinomenine hydrochloride for treat-to-target therapy of rheumatoid arthritis via modulation of proinflammatory cytokines, J. Control. Release 348 (2022) 42−56.
[18] M. Ge, C. Du, Preparation process of shear thickening gel based on constrained uniform mixture design and orthogonal experimental design, Polym. Test. 129 (2023), 108267.
[19] B. Liu, W. Wang, J. Fan, et al., RBC membrane camouflaged Prussian blue nanoparticles for gamabutolin loading and combined chemo/photothermal therapy of breast cancer, Biomaterials 217 (2019), 119301.
[20] C. He, W. Quan, Y. Zeng, et al., Construction of nicotinic acid curcumin nanoparticles and its Anti-atherosclerosis effect via PCSK9/LDL-R, ABCA1/Caveolin-1/LXR pathway, Mater. Des. 229 (2023), 111931.
[21] L. Concha, A.L. Resende Pires, A.M. Moraes, et al., Cost function analysis applied to different kinetic release models of Arrabidaea chica verlot extract from chitosan/alginate membranes, Polymers 14 (2022), 1109.
[22] P. You, A. Yang, Y. Sun, et al., Pro-efferocytosis biomimetic nanocomplexes for targeted atherosclerosis therapy through promoting macrophage re-polarization and inhibiting senescence, Mater. Des. 234 (2023), 112316.
[23] S. Hu, Y. Lin, C. Tong, et al., A pH-Driven indomethacin-loaded nanomedicine for effective rheumatoid arthritis therapy by combining with photothermal therapy, J. Drug Target. 30 (2022) 737−752.

Fig. 9. Safety evaluation of hyaluronic acid (HA)-modified hybrid membrane (M)-camouflaged poly lactic-co-glycolic acid (PLGA) loaded halofuginone hydrobromide (HF) nanoparticles (NPs) (HA-M@P@HF NPs) in vivo. (A−H) Complete blood panel analysis of white blood cell (WBC) (A), neutrophil (NEU) (B), monocyte (MONO) (C), lymphocyte (LYM) (D), hematocrit (HCT) (E), hemoglobin (HGB) (F), platelet (PLT) (G), and PLT distribution width (PDW) (H) levels. (I−L) Evaluation of hepatotoxicity and nephrotoxicity by measuring plasma levels of alanine transaminase (ALT) (I), aspartate aminotransferase (AST) (J), blood urea nitrogen (BUN) (K), and creatinine (Cr) (L). (M) Hematoxylin-eosin (H&E)-stained heart, liver, spleen, lung, and kidney tissue sections from normal control rats and adjuvant-induced arthritis (AIA) rats of different treatment groups. Data are presented as mean ± standard deviation (n = 3). *P < 0.05, **P < 0.01, and ***P < 0.001. MTX: methotrexate.

[24] S. Alivernini, L. MacDonald, A. Elmesmari, et al., Distinct synovial tissue macrophage subsets regulate inflammation and remission in rheumatoid arthritis, Nat. Med. 26 (2020) 1295−1306.

[25] S. Tardito, G. Martinelli, S. Soldano, et al., Macrophage M1/M2 polarization and rheumatoid arthritis: A systematic review, Autoimmun. Rev. 18 (2019), 102397.

[26] M. Hu, Z. Yao, L. Xu, et al., M2 macrophage polarization in systemic sclerosis fibrosis: Pathogenic mechanisms and therapeutic effects, Heliyon 9 (2023), e16206.

[27] H. Li, Y. Feng, X. Zheng, et al., M2-type exosomes nanoparticles for rheumatoid arthritis therapy via macrophage re-polarization, J. Control. Release 341 (2022) 16−30.

[28] M. Noack, P. Miossec, Selected cytokine pathways in rheumatoid arthritis, Semin. Immunopathol. 39 (2017) 365−383.

[29] T. Huang, N. Mu, J. Gu, et al., DDR2-CYR61-MMP1 signaling pathway promotes bone erosion in rheumatoid arthritis through regulating migration and invasion of fibroblast-like synoviocytes, J. Bone Miner. Res. 34 (2019) 779−780.

[30] P.D. Katsikis, C.Q. Chu, F.M. Brennan, et al., Immunoregulatory role of interleukin 10 in rheumatoid arthritis, J. Exp. Med. 179 (1994) 1517−1527.

[31] H. Matsumoto, Y. Fujita, T. Asano, et al., Association between inflammatory cytokines and immune-checkpoint molecule in rheumatoid arthritis, PLoS One 16 (2021), e0260254.

[32] K.S. Nandakumar, Q. Fang, I. Wingbro Ågren, et al., Aberrant activation of immune and non-immune cells contributes to joint inflammation and bone degradation in rheumatoid arthritis, Int. J. Mol. Sci. 24 (2023), 15883.

[33] J.G. Navashenaq, A.G. Shabgah, M. Hedayati-Moghadam, et al., The role of myeloid-derived suppressor cells in rheumatoid arthritis: An update, Life Sci. 269 (2021), 119083.

[34] H.J. Kim, B. Ohk, H.J. Yoon, et al., Docosahexaenoic acid signaling attenuates the proliferation and differentiation of bone marrow-derived osteoclast precursors and promotes apoptosis in mature osteoclasts, Cell. Signal. 29 (2017) 226−232.

[35] I.P. Perpétuo, J. Caetano-Lopes, A.M. Rodrigues, et al., Effect of tumor necrosis factor inhibitor therapy on osteoclasts precursors in rheumatoid arthritis, BioMed Res. Int. 2017 (2017), 2690402.

[36] K.A. Lee, K.W. Kim, B.M. Kim, et al., Promotion of osteoclastogenesis by IL-26 in rheumatoid arthritis, Arthritis Res. Ther. 21 (2019), 283.

[37] J.S. Smolen, R.B.M. Landewé, J.W.J. Bijlsma, et al., EULAR recommendations for the management of rheumatoid arthritis with synthetic and biological disease-modifying antirheumatic drugs: 2019 update, Ann. Rheum. Dis. 79 (2020) 685−699.

[38] X. Zhang, Y. Liu, W. Liu, et al., Macrophage-hitchhiking interleukin-10 plasmid DNA delivery system modulates rheumatoid arthritis microenvironment via the re-polarization of macrophages, Nano Today 54 (2024), 102068.

[39] S. Li, J. Li, Y. Zhao, et al., Supramolecular integration of multifunctional nanomaterial by mannose-decorated azocalixarene with ginsenoside Rb1 for synergistic therapy of rheumatoid arthritis, ACS Nano 17 (2023) 25468−25482.

[40] Z. Tang, Z. Meng, X. Yang, et al., Neutrophil-mimetic, ROS responsive, and oxygen generating nanovesicles for targeted interventions of refractory rheumatoid arthritis, Small 20 (2024), e2307379.

[41] C. Tao, F. Li, Z. Ma, et al., Highly efficient oral iguratimod/polyvinyl alcohol nanodrugs fabricated by high-gravity nanoprecipitation technique for treatment of rheumatoid arthritis, Small (2024), e2304150.

[42] D.K. Kim, J.Y. Park, Y.J. Kang, et al., Drug repositioning of metformin encapsulated in PLGA combined with photothermal therapy ameliorates rheumatoid arthritis, Int. J. Nanomedicine 18 (2023) 7267−7285.

[43] T. Puidokas, M. Kubilius, A. Stumbras, et al., Effect of leukocytes included in platelet concentrates on cell behaviour, Platelets 30 (2019) 937−945.

[44] A. Nakashima, K. Suzuki, H. Fujii, et al., POS0527 acute kidney injury (AKI) in patients with rheumatoid arthritis (RA), Ann. Rheum. Dis. 80 (2021), 497.